Version of Record: https://www.sciencedirect.com/science/article/pii/S1359645422000118
Manuscript_f3fb65a6fd9c51ec14afc2aa65fda100

Development of grain-scale slip activity and lattice rotation fields in Inconel 718

Jonathan M. Hestroffer[1,a], Marat I. Latypov[b], Jean-Charles Stinville[a], Marie-Agathe Charpagne[a], Valery Valle[c], Matthew P. Miller[d], Tresa M. Pollock[a], Irene J. Beyerlein[a,e]

[a] *Materials Department, University of California, Santa Barbara, CA, USA*
[b] *Department of Materials Science and Engineering, University of Arizona, Tucson, AZ 85721, USA*
[c] *Institut PPRIME, Université de Poitiers, CNRS, ENSMA, UPR 3346, Chasseneuil Cedex 86962, France*
[d] *Mechanical and Aerospace Engineering, Cornell University, Ithaca, NY USA*
[e] *Department of Mechanical Engineering, University of California, Santa Barbara Santa Barbara, CA, USA*

Abstract

Using a combination of in-situ high-resolution digital image correlation (HR-DIC), Heaviside-DIC method (H-DIC), and crystal plasticity finite element (CPFE), we investigate the evolution of intragranular lattice rotations and slip activity during monotonic and cyclic loading in a high performance, polycrystalline face centered cubic material. The CPFE employs a quasi-3D model microstructure, which is a highly resolved mirror representation of the experimental in-situ test sample. In agreement, the measurements and calculations reveal that most grains, regardless of their size and lattice orientation, develop intragranular lattice rotation gradients that span the grain. For a small cluster of grains on the deformed material, we perform HR-DIC analysis of slip lines to demonstrate agreement in the active slip systems and changes in this local slip activity across the individual grains. The combined analysis reveals that deforming grains are divided into sub-granular regions of uniform lattice rotation and these regions are most often associated with only one or two active slip systems. The gradient lines that divide them correspond to changes

*corresponding author: jonathanhestroffer@ucsb.edu
Email address: jonathanhestroffer@ucsb.edu (Jonathan M. Hestroffer)

in the predominant slip system. The model is used to examine the evolution of intragranular lattice rotation in a single fully reversed tension-compression cycle. The calculations indicate that intragranular gradients intensify during the reverse loading path as nearest neighboring regions appear to shed lattice rotation, increasing the lattice rotation in some regions, while shutting down rotation in neighboring regions. These findings provide insight into the irreversible changes that develop within deforming grains at the scale of the grain, particularly the heterogeneous development of intragranular lattice rotation in early stages of deformation, which could serve as precursors to localization.

Keywords: Crystal Plasticity; High-Resolution Digital Image Correlation; Superalloys; Microstructure; Grain Boundaries

---

1. Introduction

Due to their superior strength and creep resistance at elevated temperatures, nickel-based superalloys are the most common materials used in the hot section of gas turbine engines [1]. Under mechanical monotonic or cyclic strain, slip can localize within individual grains, creating bands that serve as precursors for cracks [2–5]. Statistical and computational analyses have shown that their locations are correlated with properties of the grains, including lattice orientation-dependent elasticity and slip, as well as subgrain features, such as proximity to triple junctions, sharp corners, and twin boundaries [6, 7]. The dependence of these bands on the geometric and mechanical properties of the grain structure underlines the importance of understanding the spatial distribution of stress, strain, and active slip at the subgrain scale.

To accommodate plastic strain in polycrystalline face-centered cubic (FCC) materials through crystallographic slip, slip must proceed by some combination of twelve available and distinct slip systems. This constraint, together with the requirement to maintain deformation compatibility across grain boundaries, results in non-uniform fields of stress, strain, and lattice rotation across the grain structure [8]. Lattice rotation represents a reorientation of the crystal lattice

as a direct consequence of slip activity, the number of active slip systems and distribution of slip among the active systems, and therefore emerges as an effective indicator of the operative deformation mechanisms. As an example, Zhou et al. used measures of lattice rotation from EBSD and micro-Laue diffraction to identify subsurface slip system activity in deformed Mg-5Y [9]. Such activity was otherwise undetectable through other surface-based techniques like high-resolution digital image correlation (HR-DIC). Recent research has also pointed to the importance of lattice rotation in understanding slip processes. Using in-situ synchrotron-based high-energy x-ray diffraction microscopy (HEDM), Miller et al. studied the evolution of intragranular lattice misorientation in copper during cyclic loading [10]. They reported significant evolution and irreversibility of misorientation as early as the second cycle, as a result of the development of spatial heterogeneity in inelastic deformation mechanisms within the grains. Previous work by Di Gioacchino et al. studied the development of heterogeneous lattice rotation fields and accompanying slip activity in 304L stainless steel, subject to monotonic tensile loading, using EBSD and HR-DIC experiments respectively [11]. There, they reported that the grain interiors in 304L alloy form distinct domains of deformation separated by gradients in lattice rotation.

Spatially resolved computational methods, such as full-field crystal plasticity finite element (CPFE) and viscoplastic Fast Fourier transform (CPFFT) methods can calculate inter- and intragranular fields of both slip activity and lattice rotation [12, 13]. The type of formulation used in this work, CPFE, combines physically-based theories of plastic flow, represented in a continuum framework, with the numerical finite-element method, allowing for a full-field spatial mapping of stress, strain, and lattice rotation based on microstructure, elastic anisotropy, and underlying slip processes [12].

While intragranular lattice rotation is readily calculable by CPFE, the same measure is less directly obtainable in conventional DIC experiments as the total strain computed is a convolution of elastic and plastic strains. With the introduction of high-resolution (HR-DIC) measurements and the discontinuity-

tolerant Heaviside-DIC method (H-DIC), it is now possible to isolate the non-localized strain field from the displacement discontinuities that arise from discrete slip or shearing events and the resultant lattice rotation fields [14, 15]. The lattice rotation field calculated with this method is both more accurate and presents a better physical analog to CPFE lattice rotation calculations than conventional DIC. While EBSD has been adapted for the measurement of lattice rotation, such measurements do not provide the location and intensity of slip and identification of the active slip systems. HR-DIC and H-DIC methods can capture both slip activity and lattice rotation during loading without the need to perform EBSD measurements during each loading step, allowing for the measurement of lattice rotation evolution during loading. In addition, the measurement of lattice rotation by HR-DIC provides a spatial relation between slip and lattice rotation gradients, which is not possible by EBSD measurement.

Many studies have compared the resolved micromechanics fields between full-field crystal plasticity models and DIC experiments [16–20]. Of these a few of them have studied lattice rotation and slip system activation [21–27], typically with the aim to evaluate model performance. Comparisons involving single crystal and oligocrystal specimens, in most cases, achieve good agreement, both qualitative and quantitative [21, 23, 28]. Lim and co-authors investigated development of lattice rotation fields in columnar-grain oligocrystals of Ta via HR-DIC and a quasi-3D, extruded CPFE model. Their model accurately predicted the resulting strain fields as well as misorientation at a subgranular level. This level of agreement was attributed to a high fidelity reconstruction of the initial microstructure in the model [21]. Through comparisons of intragranular misorientations from HR-DIC and CPFE Ti-6l-4V, Zhang et al. proposed a relationship between complex wavy slip and the activation of basal and prismatic slip systems [23]. With 3D EBSD and CPFE, Zaafarani et al. mapped the development of lattice rotations in a few grains of Cu after nanoindentation, revealing large orientation gradients across the plastic zone formed by the indenter [27]. While the model produced magnitudes of rotation consistent with experiment, discrepancies in the finer intragranular distributions, particular changes in the

sign of rotation were noted.

Further, when modeling more general polycrystalline microstructures, however, relatively greater deviations between experiment and model have been reported. Work by Githens et al. [26], studied slip activity in polycrystalline magnesium alloy WE43, comparing results of DIC experiments with that of quasi-3D, as well as 3D CPFE models with generated subsurface grain structures. Neither model was able to achieve the level of agreement in resolved fields like those in single crystals or oligo-crystals, and attributed the observed deviations to both lack of the full-3D microstructure information and unknown 3D boundary conditions. Pokharel et al. [22] tracked the evolution of lattice rotation within an HEDM-acquired 2D slice of internal microstructure of a copper tensile specimen. The CPFFT columnar-grained model, created from the reconstructed slice, showed good agreement in the grain-average lattice rotations, but predicted rotation gradients at grain boundaries, and not in the interior of the grains, as observed experimentally. Correct prediction of the patterns of lattice rotation in a polycrystal array is a critical test of crystal plasticity models and associated boundary conditions.

In this work, direct comparisons of highly resolved intragranular lattice rotation and slip activity are made between in-situ HR-DIC experiment and a full field crystal plasticity model in order to understand heterogeneous development of intragranular lattice rotation in early stages of monotonic deformation as well as gain insight into the evolution of intragranular lattice rotation during cyclic loading. To facilitate direct point-by-point comparisons of measured and calculated intragranular fields, the analysis involves highly resolved spatial maps of lattice rotation from in-situ HR-DIC deformation and CPFE for the same microstructure, at the same fine resolution, and under the same boundary conditions. The model captures sub-grain features of the lattice rotation fields observed experimentally, including the gradients in the amount and sign of lattice rotation within individual grains, as well as across multiple grains. Analysis of the associated local slip activity reveals that individual grain deformation proceeds primarily by dividing into domains of distinct single or dual slip. We find

that the observed intragranular gradients, which are associated with a change in the sign of lattice rotation, result from transitions in the primary active slip system. The calculations forecast that, during a tension-compression loading cycle, the misorientation across these intragranular gradients increase, implying that intragranular orientation gradients would progressively increase under cyclic loading.

The paper is structured as follows. It begins with a description of the experimental and modeling methods, focusing on calculation of lattice rotations. This is followed by direct comparisons of the measured and calculated lattice rotation fields within grains and across groups of grains. Next, the relationship between the lattice rotation fields and the underlying slip activity is analyzed and accompanied with a discussion on the evolution of lattice rotation and gradients in lattice rotation upon cyclic loading in the material, and local analysis of slip activity with H-DIC and the model. The paper concludes with a discussion of the possible sources for the few discrepancies seen between calculations and measurement.

2. Materials and Methods

2.1. Materials

The material investigated is a precipitation strengthened polycrystalline nickel-based superalloy IN718. The nominal composition is Ni - 0.56 %Al - 17.31%Fe - 0.14%Co - 17.97%Cr - 5.4%Nb - Ta-1.00%Ti - 0.023%C - 0.0062%N (wt%). The material was heat treated to produce large grain size and a high γ"-phase content. Thermal processing began with a solution annealing step, 30 min at 1050°C followed by water quench. Afterwards, the material underwent precipitation hardening, which entails 8 h at 720°C followed by 8 h at 620°C.

Prior to deformation, scanning electron microscope (SEM) images and electron backscatter diffraction (EBSD) maps were acquired. EBSD measurements were performed with an EDAX OIM-Hikari XM4 EBSD detector using a step size of 0.7 μm. Diffraction patterns were acquired using an accelerating volt-

age of 20 kV, a 2×2 binning and a beam current of 0.2 nA. The chemical-mechanical polishing consisted of mechanical polishing with SiC papers up to 1200 grit, following by polishing with a 6 μm diamond suspension and then chemo-mechanical polishing with 0.05 μm colloidal silica for 12 hours. Fig. 1a shows the representative grain structure characterized by EBSD. The average grain size is 62 μm.

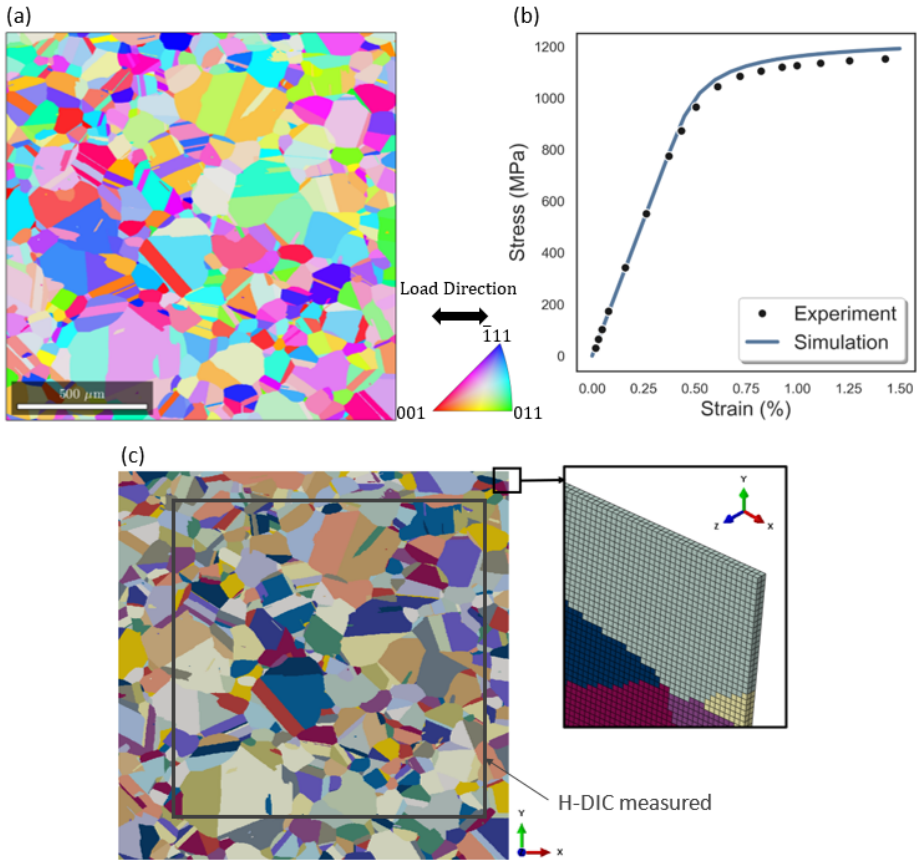

Figure 1: Inverse pole Fig. map along the loading direction of the IN718 alloy (a), engineering stress-strain curves measured by experiment and simulated by CPFE for the RVE (b), and finite element model of the IN718 microstructure (c). The model encompasses the entire inverse pole figure map while the gray rectangle denotes the area of the microstructure measured by HR-DIC. A magnified image of the top-right corner of the model shows thickness and resolution of the model, and a categorical color code indicates grain ID.

2.2. Experiments

Tensile testing was performed at room temperature using a custom in-situ 5000 N stage within a FEI Versa3D on flat dog bone-shaped specimens with a gauge section of 1×3 mm^2. Macroscopic strains were measured in situ using fiducial markers located at both ends of the gauge length. The axial loading direction is horizontally oriented in all maps shown here. Fig. 1b shows the stress-strain response of this sample up to a strain of 1.5%.

The test continued until a macroscopic strain of 1.83% where it was interrupted for high-resolution HR-DIC measurements. The speckle pattern used for these measurements was applied by gold nanoparticle deposition with an average particle size of 60 nm [29]. Direct spatial registration between the SEM images, the DIC strain maps and the EBSD maps is performed using pairs of control points, mostly located on triple points, as described in [5]. To minimize distortion errors, approximately 70 control points were selected over the areas of interest. To reduce imaging distortions, high magnification images were taken at horizontal field widths of 138 μm. To reduce drift distortions, large electron beam spot sizes and large dwell times (20 μs, 6 min per image) were used. In addition, to minimize charging effects, low acceleration voltages of 5 kV were employed [30]. For the strain calculations, tiles of 10×10 images before and after deformation with an image overlap of 15% were used. The results are merged using a pixel resolution merging procedure given in [31]. With the HR-DIC images collected during testing, additional data reduction using the Heaviside-DIC method (H-DIC) was performed [14]. With the HR-DIC measurements of in-plane displacement fields at the surface of the deformed specimen, the Heaviside-DIC method separates the displacements induced by discontinuities and gradients of displacement [14, 15]. The lattice rotation field around discontinuities, here slip localizations, that physically correspond to in-plane lattice rotation can be calculated utilizing the first gradient of the displacement field. The approach used to extract the rotation from HR-DIC measurement is described elsewhere [15]. For HR-DIC, we chose to investigate regions of 1×1 mm^2. Subset size of 31×31 pixels (1044×1044 nm^2) with a step size of 3 pixels

(101 nm) were used for DIC measurements. The sample preparation, imaging conditions and Heaviside-DIC parameters allow for a discontinuity detection resolution between 0.2 and 0.3 pixels (7 nm and 10 nm respectively) [14].

2.3. Computational Modeling Background

The CPFE model used in this study adopts the constitutive law developed by Kalidindi, Bronkhorst, and Anand [32]. Minor modifications were made to incorporate strain hardening via a dislocation density based hardening law. The kinematics and constitutive law defined in the model were introduced in the form of a user-defined mechanical material behavior (UMAT) subroutine implemented in ABAQUS/Standard, as described in more detail in the following section.

Kinematics and Constitutive Law

The kinematics of the model are shown below, following closely the notation used by Asaro [33]. Here, tensor and vector quantities are denoted by bold-faced uppercase and lowercase letters respectively. All other terms are scalars. Through multiplicative decomposition, the total deformation gradient tensor, $\mathbf{F}$, can be separated into elastic, $\mathbf{F}^*$, and plastic, $\mathbf{F}^p$, deformation gradient tensors as, $\mathbf{F} = \mathbf{F}^*\mathbf{F}^p$. Here, following the conventional definition, we refer to *lattice rotation* as the orthogonal part of the elastic deformation gradient tensor [34–36], i.e.,

$$\mathbf{F}^* = \mathbf{R}^*\mathbf{U}^* \tag{1}$$

where $\mathbf{R}^*$ is the lattice rotation tensor, and $\mathbf{U}^*$ the right elastic stretch tensor. We should note that in the present study, the plastic strains are sufficiently small, such that it is reasonable to assume plastic deformation manifests solely as crystallographic slip.

The velocity gradient tensor, $\mathbf{L}^p$ is related to $\mathbf{F}^p$ via, $\mathbf{L}^p = \dot{\mathbf{F}}^p{\mathbf{F}^p}^{-1}$. The rate of plastic deformation is then specified by the sum of slip rates on all slip systems in tensorial form

$$\mathbf{L}^p = \sum_{\alpha=1}^{n} \dot{\gamma}^{(\alpha)} \left(\boldsymbol{s}^{(\alpha)} \otimes \boldsymbol{m}^{(\alpha)} \right) \tag{2}$$

where, $\dot{\gamma}^{(\alpha)}$, represents the slip rate on slip system α and $\boldsymbol{s}^{(\alpha)}$ and $\boldsymbol{m}^{(\alpha)}$ represent unit slip system direction and normal vectors, respectively. In this model, slip rates on each system are given by a rate-dependent power-law similar to that suggested by Peirce, Rice and Needleman [37]

$$\dot{\gamma}^{(\alpha)} = \dot{\gamma}_0 \left| \frac{\tau^{(\alpha)}}{g^{(\alpha)}} \right|^n sgn\left(\tau^{(\alpha)}\right) \tag{3}$$

where $\dot{\gamma}_0$ represents the reference slip rate, $\tau^{(\alpha)}$ the resolved shear stress on slip system α, $g^{(\alpha)}$ the slip resistance on system α, and n the power-law exponent. Slip resistance evolves according to a generalized matrix form of the classic Taylor relation suggested by Franciosi et al. [38] taking into account the average interaction strengths between slip systems, given as follows

$$g^{(\alpha)} = g_0 + \alpha b \mu \sqrt{\sum_{\beta=1}^{n} a^{\alpha\beta}\, \rho^{(\beta)}} \tag{4}$$

where g_0 is a constant resistance that does not evolve with strain, α a statistical dislocation interaction coefficient equal to unity, b the value of the Burgers vector, μ the shear modulus, $a^{\alpha\beta}$ a slip-interaction matrix with diagonal components capturing self-hardening and off-diagonal ones representing latent hardening, and $\rho^{(\beta)}$ the dislocation density on system β. The dislocation density evolution is calculated according to the Kocks-Mecking equation [39], composed of a positive storage rate term and a negative dynamic recovery term

$$\dot{\rho}^{(\alpha)} = \frac{1}{b} \left(\frac{1}{K} \sqrt{\sum_{\beta=1}^{n} a^{\alpha\beta}\, \rho^{(\beta)}} - 2 y_c \rho^{(\alpha)} \right) \left| \dot{\gamma}^{(\alpha)} \right| \tag{5}$$

where K is a scalar that scales with the average strength of the dislocation-dislocation junctions, and y_c is the critical annihilation distance.

Constitutive Model Parameters

Table 1 lists the relevant constitutive model parameters for IN718. Values for elastic constants and initial dislocation density of IN718 were obtained from the literature [40]. The only model parameter that is adjusted to agree with the entire measured stress-strain curve is g_0. A $10 \times 10 \times 10$ finite element representative volume element (RVE) of the material was generated for calibration. The model consisted of 1000, eight-noded cubic mesh elements, each element representing a single grain with a given crystallographic orientation sampled from a uniformly random orientation distribution. The RVE was tested with periodic boundary conditions in uniaxial tension. Fig. 1b overlays the calculated stress-strain response with the measured stress-strain data. Both the elastic response and hardening of the model compared well with experiment.

Table 1: Constitutive model parameters.

Parameter	Magnitude	Unit
C_{11}	259.6	GPa
C_{12}	179	GPa
C_{44}	109.6	GPa
$\dot{\gamma}_0$	10^{-3}	s^{-1}
n	20	-
g_0	400	MPa
b	0.257	nm
$\alpha^{\alpha=\beta}$	0.1	-
$\alpha^{\alpha\neq\beta}$	0.1	-
ρ_0	1.5x10^{12}	m^{-2}
K	10	-
y_c	2.57	nm

Model Microstructure and Boundary Conditions

To compare with the HR-DIC tension test results, a quasi-3D CPFE model with traction-free surfaces was constructed, simulating a generalized plane stress condition, adopting the form of Wang et al. [41].[1] To accomplish this, the raw EBSD data was first resampled at every second pixel along the horizontal and vertical direction to a reduced resolution of 1071×1066. This grid of pixels was then mapped to a grid of eight-node linear brick elements (C3D8) of equivalent resolution, followed by a small extrusion of the model to a thickness of two elements. Fig. 1c shows the resulting model microstructure. Elements belonging to the same grain according to the EBSD data were assigned the respective mean grain orientation. Uniaxial tension was applied along the x direction at a strain rate of $10^{-3}s^{-1}$ until a strain of 1.83%, simulating macroscopic strain achieved in experiment. Periodic boundary conditions were imposed in the x and y directions, while the two surfaces of the model remained traction-free. Based on initial testing of different boundary conditions, we found that these boundary conditions provided the greatest numerical stability and best representation of the material on the free surface in the DIC experiment. As an effect of the generalized plane-stress boundary conditions achieved with this model, the only significant lattice rotations that develop are those in-plane, given by the $\mathbf{R}^*_{12}$ component of the lattice rotation tensor. While such conditions are known for their greater tendency for strain localization compared to plane-strain boundary conditions, we expect the main tendencies on intragranular slip activity and lattice rotation not to differ between them.

3. Results and Discussion

3.1. Full-field Comparisons

The in-plane lattice rotations are measured at every point in the microstructure under tensile strain of 1.83%. Fig. 2a presents the experimental lattice

[1] Typically when simulating traction-free surface conditions, a 2D plane stress model is adopted. We have found such models to be numerically unstable.

rotation field map using blue shades for counter-clockwise (negative) rotations and red shades for clockwise (positive) rotations. The applied strain is sufficiently high to result in intragranular lattice rotations in most of the grains in the sample. The rotation gradients are not exclusively at grain boundaries or triple junctions. Most of the lattice rotations are 1° or less, a small fraction greater than 2°, and a rare few greater than 3°. The lattice rotation fields are calculated for the same microstructure at the same strain. In the map in Fig. 2b, we show only the calculated in-plane rotations in the surface plane of the sample for direct comparison with experimental data. Many features of the lattice rotation distribution agree with the measurement, from the long-range bands of like-signed lattice rotation spanning many grains to the short-range intragranular lattice rotation gradients. The calculated lattice rotation distribution is, however, sharper with more intense regions. This difference likely arises from the lack of nonlocal strain hardening and/or constraint of a subsurface microstructure in the model, which otherwise can slow down lattice rotation evolution.

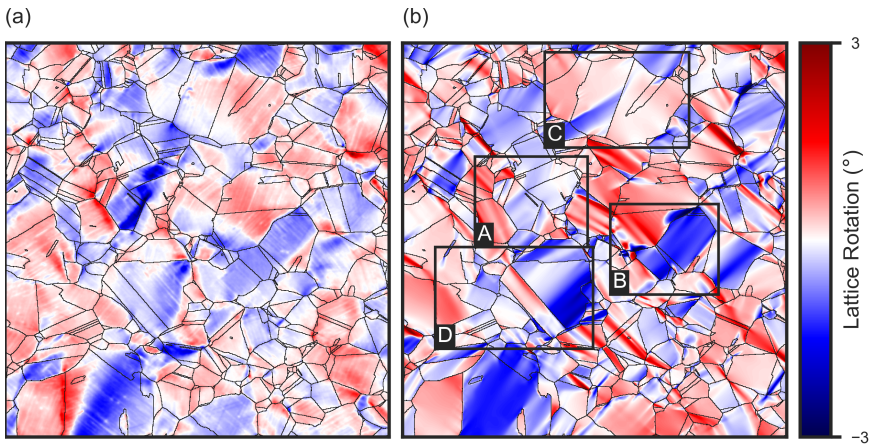

Figure 2: Comparison of lattice rotation maps for HR-DIC experiment (a) and CPFE simulation (b) with four regions of interest labelled A, B, C, and D.

The range of lattice rotations observed in the region of interest is given by the lattice rotation distributions in Fig. 3a. As expected for a uniaxial ten-

sion experiment, there is no net rotation, as exemplified in the similar amounts of positive and negative rotations across the sample. These lattice rotations, both positive and negative, are no more than 1° (the 95th percentile of the distribution). The calculated lattice rotation distribution is overlaid onto the experimental one for comparison. It is similar to the measured one, although slightly broader, with lattice rotations of 1° or less marking the 85th percentile, a reflection of the tendency for the model to predict slightly higher and sharper intensities. Also, one sub-peak is found in the simulation distribution between -1.5 and -1°. In the same rotation range, a shoulder in the experimental distribution is visible. Analysis shows that the peak corresponds to an over-prediction of negative lattice rotation by the model in several grain clusters (see Fig. 20 in Appendix).

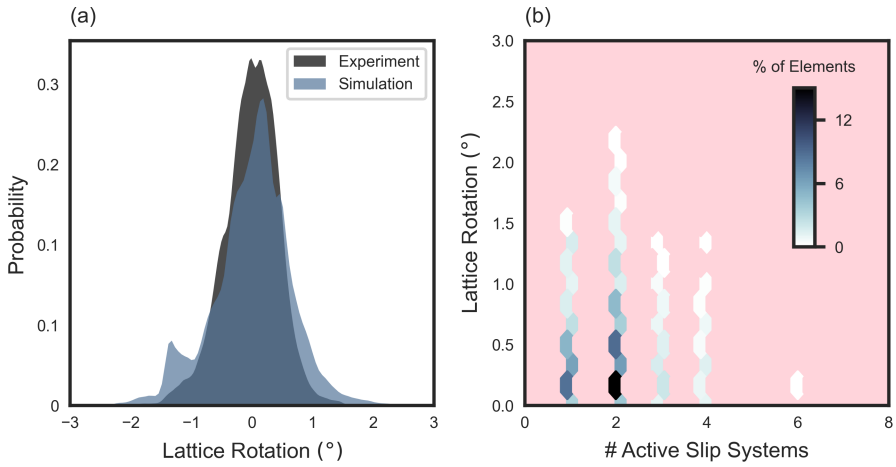

Figure 3: Probability density distributions of lattice rotation for experiment and simulation, shown in black and blue respectively, made semi-transparent to visualize regions of overlap (a). A bi-variate histogram of lattice rotation and number of active slip systems for the CPFE simulation (b).

Lattice rotations result from crystallographic slip and, in the FCC material studied here, there are 12 available slip systems. Here we define an active slip system is one that has a resolved shear stress that surpasses the initial slip resistance of 400 MPa. The number of active slip systems responsible for the

calculated lattice rotation under the applied strain of 1.83% is extracted and presented in Fig. 3b in a bi-variate plot. Again, we observe that most of the lattice rotations that develop in the model are below 1° in magnitude and further see that these are associated with double or single slip. Because they occur less frequently, the slip activity responsible for the range of lattice rotations greater than 1° is indiscernible in Fig. 3b and needs to be plotted separately, such as in Fig. 4a. Even the extreme and rare values of lattice rotations, reaching close to 3° are still associated with 1 - 2 slip systems. Therefore, one to two active slip systems are responsible for most of the lattice rotations in the model.

Lattice rotations are driven directly by slip activity but may have a relationship with the stress or strain experienced at the same material point. To identify a correlation, we use equivalent von Mises measures of stress and strain at every point and overlay the lattice rotations and their corresponding stress and strain on a map in Fig. 4b. Lattice rotations less than 2° are associated with stresses and strains that span the full range realized in the model. Only the exceptionally high rotations produced in the model within 2 to 3° can be associated with the highest von Mises strains.

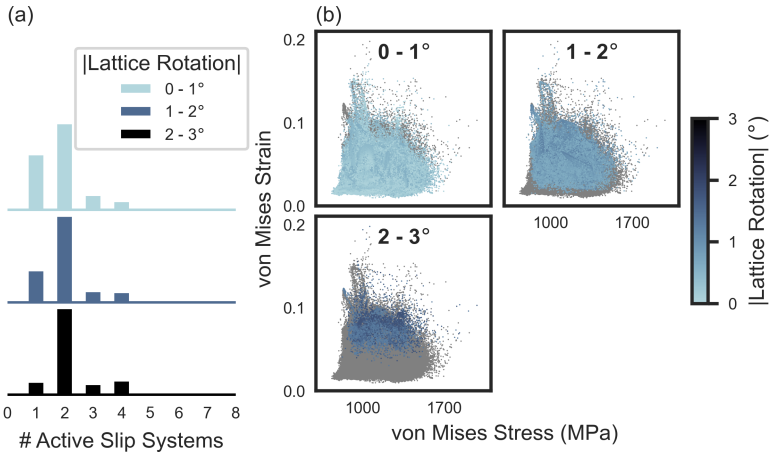

Figure 4: Probability density distributions of number of active slip systems for CPFE element populations with defined magnitude of lattice rotation (a) and Mises stress-strain relationship with lattice rotation (b). Elements outside of the selected group are colored gray and placed behind those within the group in the scatter plots.

Significantly smaller portions of the material deform by more than two active slip systems, too small to be realized in the analysis for the full range of slip activity in Fig. 4. However, the question is whether these multi-slip regions may be responsible for particularly high or low values of lattice rotation. To examine the multi-slip areas, in Fig. 5, we analyze the calculated lattice rotations within separate groups based on the number of active slip systems. Those areas with three to five active slip systems also lead to lattice rotations ranging from 2° or less, which is the same range resulting from dual or single slip. The mapping of the active slip numbers onto their von Mises stress and strain also finds no special relationship between areas operating three to five active slip systems with specific stresses or strains. The interesting finding, however, is that the small portion of material points utilizing the largest number of slip systems, six to eight, can be associated with much lower lattice rotations, less than 0.5°, and distinct values of von Mises stress.

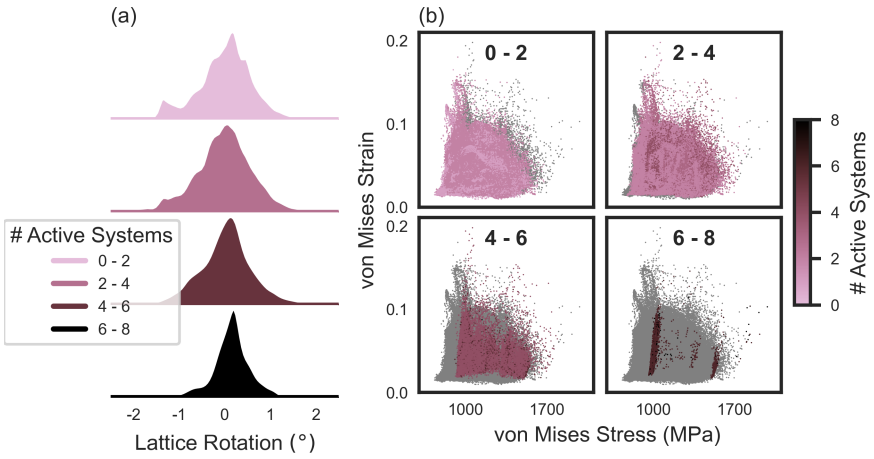

Figure 5: Probability density distributions of number of lattice rotation for CPFE element populations with defined number of active slip systems (a) and Mises stress-strain relationship with number of active slip systems (b). Elements outside of the selected group are colored gray and placed behind those within the group in the scatter plots.

From the lattice rotation fields in Fig. 2, many grains develop intragranular gradients in their interiors and not solely at the grain boundaries. In many

cases, these gradients do not have the same sign but subdivide the grain into regions of oppositely signed lattice rotation. We also find from the foregoing analysis that most material points operate one or two slip systems, and further that this single or dual slip activity can account for the full range of lattice rotations realized in the material, from the negative counter-clockwise (CCW) 2° to positive clockwise (CW) 2°. Together, these results imply that grains preferentially accommodate deformation by activating a set of few slip systems in distinct parts of the grain rather than the same set of multiple slip systems uniformly throughout the grain.

3.2. Intragranluar Rotation Fields

We examine more closely the intragranular gradients in several individual grains in Figs. 6 and 7. These groups are selected since they and their nearest neighboring grains lie fully within the sample and are not border grains in Fig. 2. For the group in Fig. 6, two intragranular gradients are generated both in experiment and the model due to a change in the sign of lattice rotation and are indicated by dashed lines marked grad_1 and grad_2. In Fig. 6b, the calculated map is shown alongside the experimental map. Even at this small scale, most of the sign changes in lattice rotation predicted by the model are in qualitative agreement with experiment. In the model, the gradients tend to be a little sharper and, in a few cases, slightly offset in their specific location in the grain but otherwise the agreement is sufficient for use in gaining further insight from the calculation. The corresponding calculated von Mises stress field is shown in Fig. 6c. There is little correlation between stress and lattice rotation in this group of grains. The stress is uniform in areas of intragranular gradients in lattice rotation. The stress is also not exceptionally low or high where these gradients lie.

Fig. 7 features other regions that also contain intragranular gradients formed by a change in sign that cuts across the grain (grad_1 and grad_2 in Fig. 7a) and two gradients in the same grain with one being near a triple junction (grad_1 and (grad_2 in Fig. 7d, e). Finally, Fig. 7h shows a group containing a ro-

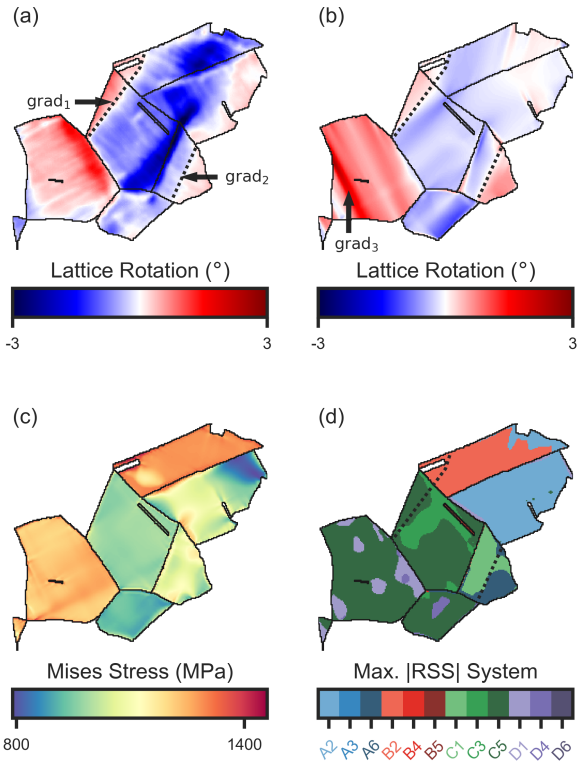

Figure 6: Maps of experimental lattice rotation (a) and CPFE calculated lattice rotation (b), von Mises stress (c), and slip systems of maximum resolved shear stress (RSS) (d) for region of interest A.

tation gradient that involves a sign change (grad_2) and another one that does not (grad_1). These close inspections clearly demonstrate that many individual grains are divided into sub-regions of lattice rotation with opposing sense.

Intragranular rotation gradients signify changes in slip properties. Since most regions operate single or dual slip, we identify only the primary system (highest slip rate) and overlap its region of activity in the microstructures in Figs. 6 and 7. Fig. 6d and Figs. 7c, f, and i present the prominent slip activity maps for all analyzed regions and in all cases they show that the intragranular gradients highlighted were caused by a change in predominant slip. Refer to Table 2 in Appendix for the slip system designation. For instance, the gradients in the two grains in Fig. 6 are attributed to a change in the predominant slip

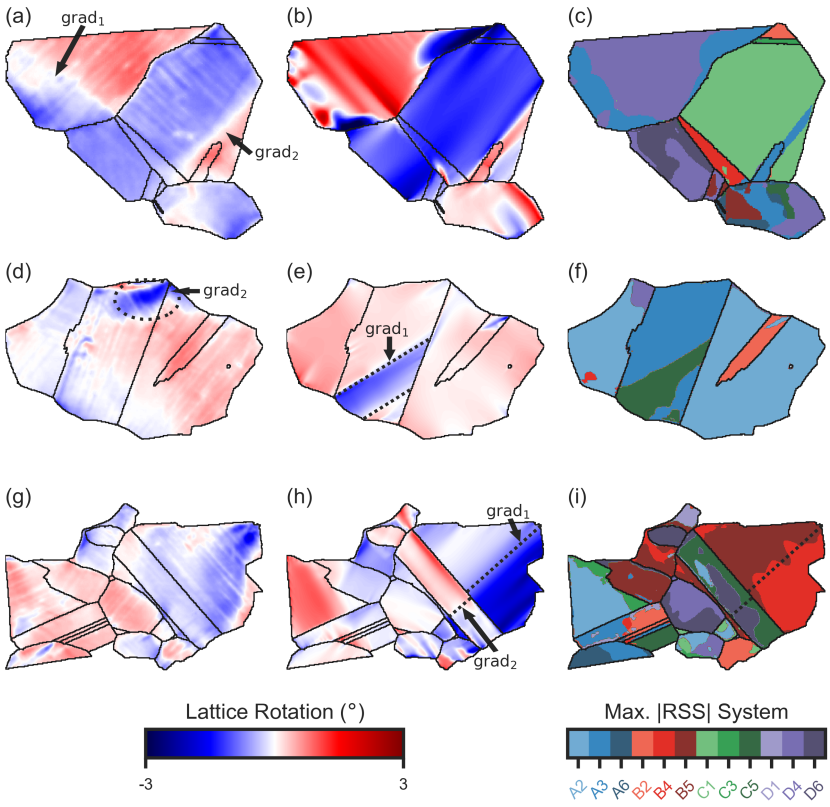

Figure 7: Maps of experimental lattice rotation, CPFE calculated lattice rotation and slip systems of maximum resolved shear stress (RSS) for regions of interest B (a-c), C (d-f), and D (g-i).

system. In Fig. 6 grad_1 in grain 1 separates areas of activity for systems C3 and C5, and grad_2 in grain 2 separates C1 and A6 activity. A Schmid factor analysis based on grain orientation and macroscopic loading alone would predict dual slip by C3/C5 in grain 1 and C1/A6 in grain 2. Yet, it is implicit that these two slip systems act in concert across the grain and not in separate regions. However, as the experiment and model clearly indicate, these grains prefer to activate different modes of slip in distinct regions, and where these regions are divided one can find gradients in lattice rotation sign. Similar results are found for the grain clusters in Fig. 7, where slip system changes responsible for these

intragranular gradients also involve a change in the glide plane not just glide direction. The $grad_2$ gradient in lattice rotation sign seen in the twin in Fig. 7i results from a non-planar slip system change, whereas the $grad_1$ gradient in lattice rotation intensity results from a planar slip system change.

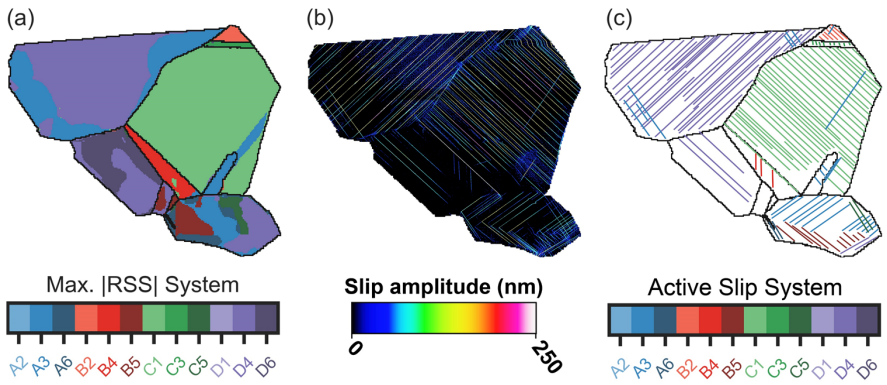

Figure 8: Maps of CPFE calculated slip systems of maximum resolved shear stress (RSS) (a), HR-DIC in-plane slip displacement (b), experimental slip activity for region of interest B.

Measurements of slip that serve as indicators of activity at the subgrain scale and at the surface can be inferred from H-DIC. For the small region in Fig. 7(a-c), we compare the calculated and measured spatial maps of active slip systems. The results in Fig. 8 show that the model is able to predict not only the locations of divergent slip activity, but also correctly identify their respective primary active slip systems. In summary, slip-mediated deformation causes grains to subdivide into separate domains of distinct lattice rotations, as a result of divergent selection of prominent slip system(s).

3.3. Cyclic Loading

For the microstructure deformed in tension, intragranular gradients are found, typically dividing grains into separate domains of lattice rotation as a result of locally divergent intragranular slip activity. Generally, slip and any effects of slip are irreversible processes, a response that would be clear when the applied straining is removed or has completely reversed. Likewise, lattice rotations,

which arise from slip, would not be expected to fully reverse in a forward-reverse strain cycle. Further, gradients in lattice rotation could be accommodated by the accumulation of geometrically necessary dislocations (GNDs) [42–44], another slip-related process, that could also contribute irreversibility. Here we investigate numerically the evolution of lattice rotation in a tension-compression cycle, but without considering any irreversibilities that could arise from GND formation.

Following the load path shown in Fig. 9, Fig. 10 shows the lattice rotation maps at four different load points during a tension-compression cycle spanning end of tension at 1.83% (1-1C) to end of compression at 1.83% (1-5C). Stage 1-2C marks the elastic-plastic transition in the subsequent compression path. During the unload/reload from 1-1C to 1-2C, only a subtle reduction in the magnitudes of the lattice rotation fields is detected. The spatial distribution and gradients in lattice rotation are retained, a possible consequence of little slip activity between these two states. At 1-3C, the macroscopic strain is zero, and, in the microstructure, the intensities in lattice rotations have noticeably reduced, a likely indication that slip in the reverse direction has begun. However, they have not disappeared and the sense of rotations, as well as gradients in rotations, still remain. Between 1-3C and 1-4C, the material has deformed beyond the theoretical yield point in compression (without the pre-tension strain). Within this increment, most of the lattice rotation field has reversed sign, signifying that the lattice rotations achieved a minimum between load points 1-3C and 1-4C. We last show the lattice rotations at 1-5C, at the compression strain of -1.83%, the same level reached at the end of the previous tensile path, 1-1C. By 1-5C, the lattice rotations have intensified in the reverse sense from those seen in 1-4C.

At 1-5C, the end of the tension-compression cycle, the lattice rotation field globally appears to have fully reversed in sign from that at the end of 1-1C. To determine whether the lattice rotations at every point have locally reversed, we calculate, for each grain, its grain average lattice rotation (GAR). Fig. 11a shows the distributions of GAR corresponding to the five stages in the tension-

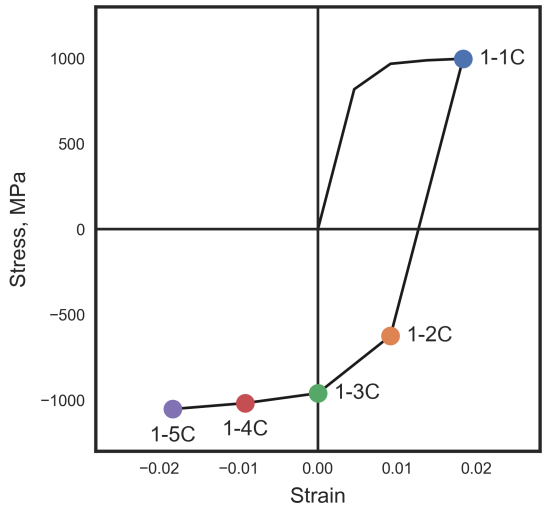

Figure 9: Stress-strain curve for the cyclic simulation with load points of interest labelled."1-1C" indicates the first tension-compression cycle at the first load point (end of tension).

compression cycle.

The GAR distribution at the peak tensile level (1-1C) is broad, spanning from 2° CCW to 2° CW. The 1-2C GAR distribution is similar, demonstrating that these lattice rotations are retained after unloading and reloading in compression to yield. The reoriented sub-crystalline regions after tension do not revert back to their initial homogeneous starting orientation at 1-2C. However, by 1-3C, when the net applied strain is zero, the GAR distributions substantially narrow and remain so, even after the sign reversal stage at 1-4C. Deformation from 1-4C to 1-5C causes lattice rotations to increase and the GAR distribution to broaden, similar to, but not completely reversed from, the distribution at 1-1C. At 1-5C, the median GAR is offset from zero toward a finite CCW rotation, indicating that some regions reorient more CCW in compression re-straining than CW in tensile pre-straining. Despite the global appearance of a fully reversed rotation field, the lattice rotations are indeed path dependent and not perfectly reversed even in the first load cycle.

Since many regions of uniform lattice rotation are not granular but sub-

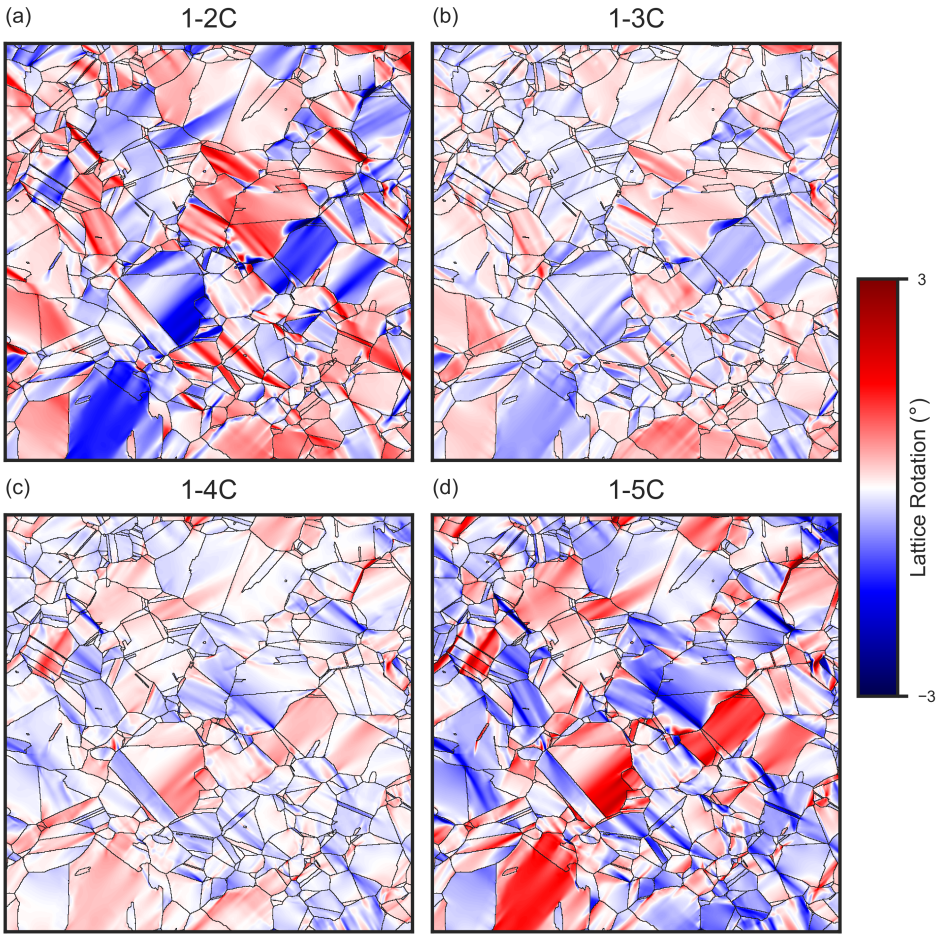

Figure 10: Maps of CPFE calculated lattice rotation for load states along the tension-compression cycle 1-2C (a), 1-3C (b), 1-4C (c), and 1-5C (d).

granular, differences in reorientation propensity between the tension path and the subsequent compression path can lead to differences in intragranular misorientation as well. In prior studies of cyclic loading tests in precipitation-hardened Cu, a grain average misorientation metric has been defined, as the misorientation between the orientation of a point relative to the average orientation [10]. Here we determine an analogous metric, based on a quaternion representation of crystal orientation, for any stage in the cycle, given by

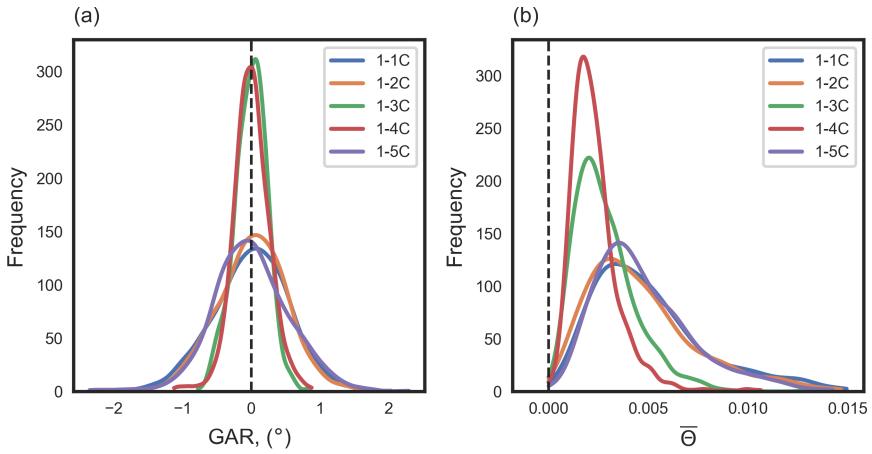

Figure 11: Histograms of grain average lattice rotation (GAR) (a) and misorientation metric $\overline{\Theta}$ (b) at each load state of the tension-compression cycle.

$$\overline{\Theta} = \frac{1}{N}\sum_{i=1}^{N}\|q_i - \overline{q}\| \tag{6}$$

which is the grain average misorientation $\overline{\Theta}$, where the misorientation is defined between the orientation of a point i in a grain q_i and the average orientation of the grain $\overline{q}$, and N is the number of points in the grain.

Fig. 11b shows the evolution of the $\overline{\Theta}$ distributions during the tension-compression cycle. The $\overline{\Theta}$ distributions generated at tension at 1-1C are broad. Unloading and reloading to compression yield point (1-2C) does not change the $\overline{\Theta}$ distribution. At 1-3C the $\overline{\Theta}$ reduces, a likely consequence of the reduction in GAR. Interestingly the $\overline{\Theta}$ becomes even lower at 1-4C after sign reversal. Despite the similar GAR distributions for 1-3C and 1-4C, the 1-4C $\overline{\Theta}$ distribution is substantially narrower than 1-3C, suggesting many of the upper tail higher misorientations at 1-3C have been removed when the lattice rotations reversed sign at 1-4C. The strain from 1-4C to 1-5C results in a substantial increase in intragranular misorientation. Like the GAR distribution, the $\overline{\Theta}$ distribution at 1-5C in compression is not the same as that at 1-1C in tension at the same strain level. A similar evolution in grain average misorientation (measured by

an in-situ HEDM) was reported in the tension to compression cycle in Cu [10]. As seen here, in their work, the intragranular distribution becomes narrower after the compression reload than that at the end of the tension reload.

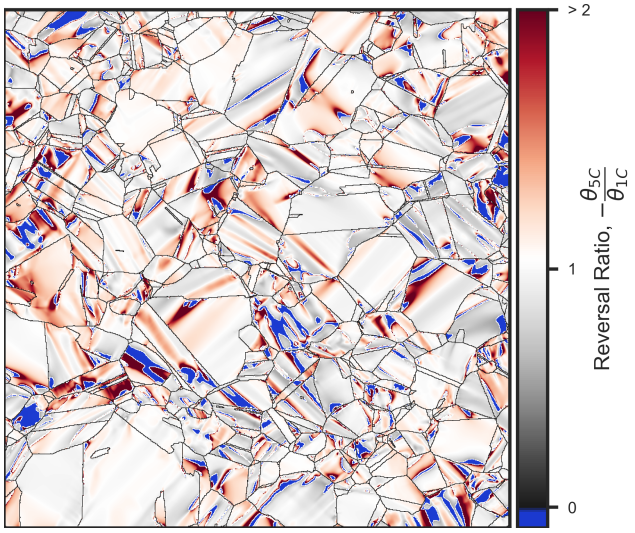

Figure 12: Map of lattice rotation reversal calculated as the negative ratio of rotations at compression (1-5C) and tension (1-1C), $R = -\dfrac{\theta_{5C}}{\theta_{1C}}$. $R < 0$ *no reversal*, $0 \leq R > 1$ *under-reversed*, $R = 1$ *fully-reversed*, $R > 1$ *over-reversed*.

To determine rotational reversal, we calculate the negative ratio of rotations at 1-5C at compression and 1-1C at tension. Fig. 12 shows a reversal ratio map of the material at the end of compression 1-5C. In this map, when the lattice rotation at a point has reversed, shades of gray identify ratios less than one, an under-reversal, and shades of red identify ratios greater than one, an over-reversal. Blue indicate a ratio less than zero indicating that the lattice rotation retained the same sign. If all points experience perfect reversal, then the map would be entirely white. Instead, as shown in Fig. 12, perfect reversals are rare. Most of the material experiences an under reversal. This would explain the narrower $\overline{\Theta}$ distribution after 1-5C compared to 1-1C. Interesting points are the smaller and fewer regions that manifest as composite bands that pair a band of severe over reversal with a band of no reversal. These bands develop along intragranular gradients that form a boundary between two domains of oppositely

signed lattice rotations. Fig. 13 identifies where composite bands of lattice rotation reversal correspond to bands of polarized gradients, i.e. gradients of opposing rotation sign, in the model for regions A and B. In Fig. 13c, while not corresponding to a composite band in the model, grad_1 clearly intensifies undergoing substantial over-reversal. Thus, the polarized intragranular gradients formed under forward loading are regions that experience significantly different slip distribution in reverse loading, causing one side to "shed" re-orientation to the other side. This phenomenon results in irreversible changes in intragranular orientation gradients.

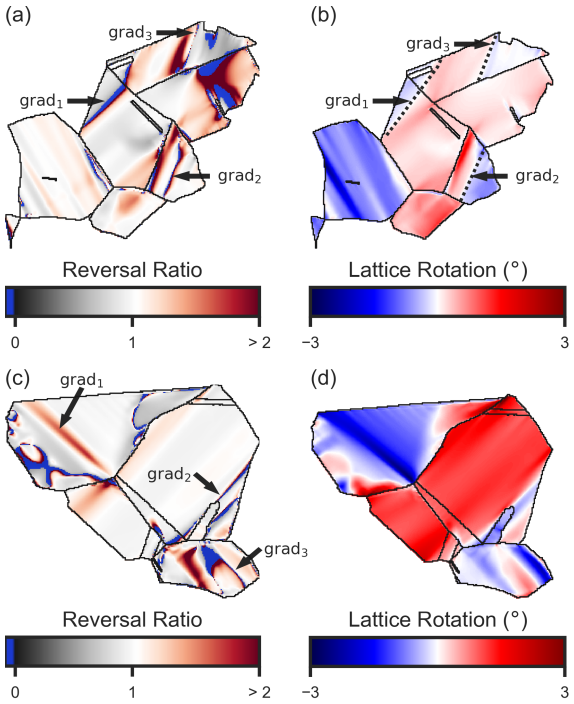

Figure 13: Maps of lattice rotation reversal and lattice rotation at end of compression (1-5C), for regions of interest A (a, b) and B (c, d).

3.4. Cyclic Loading Experiments

Another HR-DIC/CPFE comparison was performed for another microstructure for the same IN718 material. The cyclic loading conditions applied con-

sisted of first tension to 2% macroscopic strain followed by an unload where the HR-DIC measurements were taken. After, subsequent compression was applied to a macroscopic strain of -0.63% followed by another unload where another set of HR-DIC measurements were taken at a final macroscopic residual strain of 0.25%. Experimental results are available at every unload for 10 whole cycles, where as only one cycle was tested with the CPFE model. Figs. 14 and 15 show the measured and calculated lattice rotation maps for two example microstructural regions after the first tension and compression unloads. Overall, the model predicts reasonably well the lattice rotations on average per grain, and in most areas, the location and sign of the intragranular lattice rotation gradients. Agreement is better in more areas after tension and before reverse loading than after compression. We only note that during the compression cycle, in some areas of the microstructure, the lattice rotation fields of the model generally tend to reverse more than what is observed in experiment. Nevertheless, most of the map is qualitatively in agreement, sufficient for more in depth analysis.

As done in the previous section, the lattice rotation reversal ratio after one cycle was analyzed for the regions of microstructure selected. For this experiment, because of the smaller macroscopic strain achieved during the reverse loading path, full rotation reversal is not expected for most of the microstructure, therefore regions with a rotation reversal ratio approaching and surpassing unity represent locations within the material experiencing significant rotation reversal, disproportionate to the relative macroscopic strains applied. Results of this analysis show that the intragranular gradients in lattice rotation sign correspond to regions of over-reversal as exhibited in Figs. 16 and 17 where bands of significant reversal ratio, (≥ 1), track the gradient lines. On either side of these gradients as well, are regions of very low reversal indicating shedding of lattice rotation is occurring and that these gradients may intensify with further cycling. By comparing these experimental results with those after 10 cycles, both gradients analyzed are found to intensify with further cycling, confirming the original hypothesis. A final interesting finding from the analysis is the development of

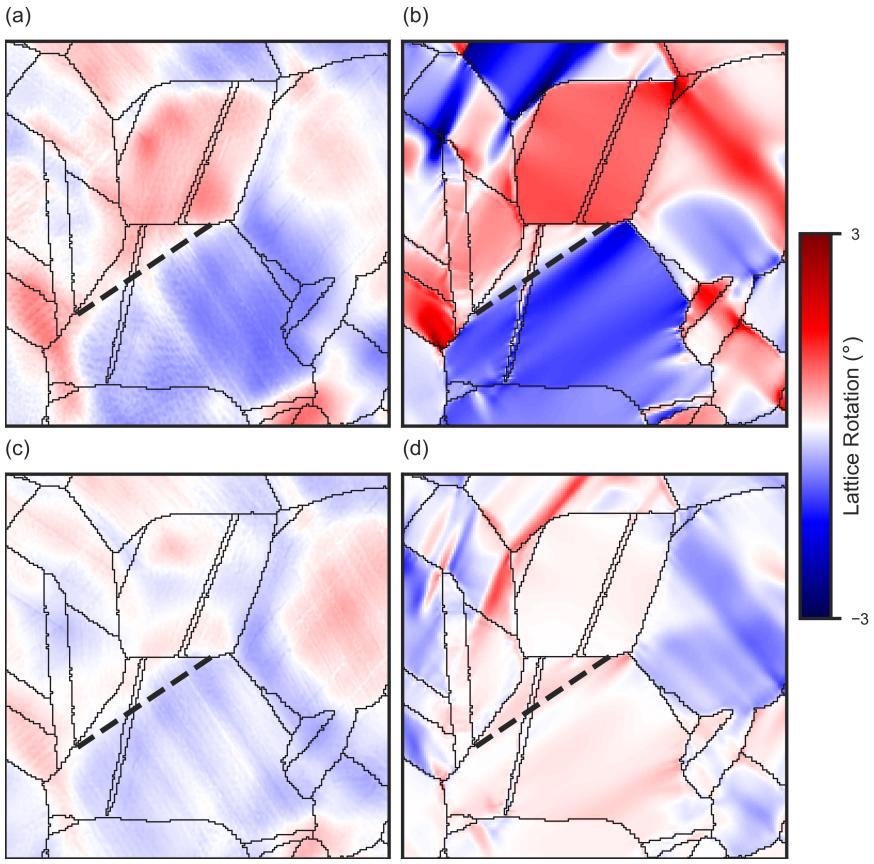

Figure 14: Maps of (a) experimental and (b) CPFE calculated lattice rotation for a region of microstructure after the first tension unload, and (c) experimental and (d) CPFE calculated lattice rotation maps after the first compression unload. The dashed line indicates the location of a polarized lattice rotation gradient.

regions of over-reversal in lattice rotation. These special regions are seen in both simulation and experimental results and may be counterintuitive since the load path is asymmetric and much less macroscopic strain is applied during reverse loading. They provide a direct indication that Ni-based superalloys exhibit slip activity that is different during reverse loading than forward loading. They are consistent with the slip irreversibility behavior of IN718 reported in [15, 45].

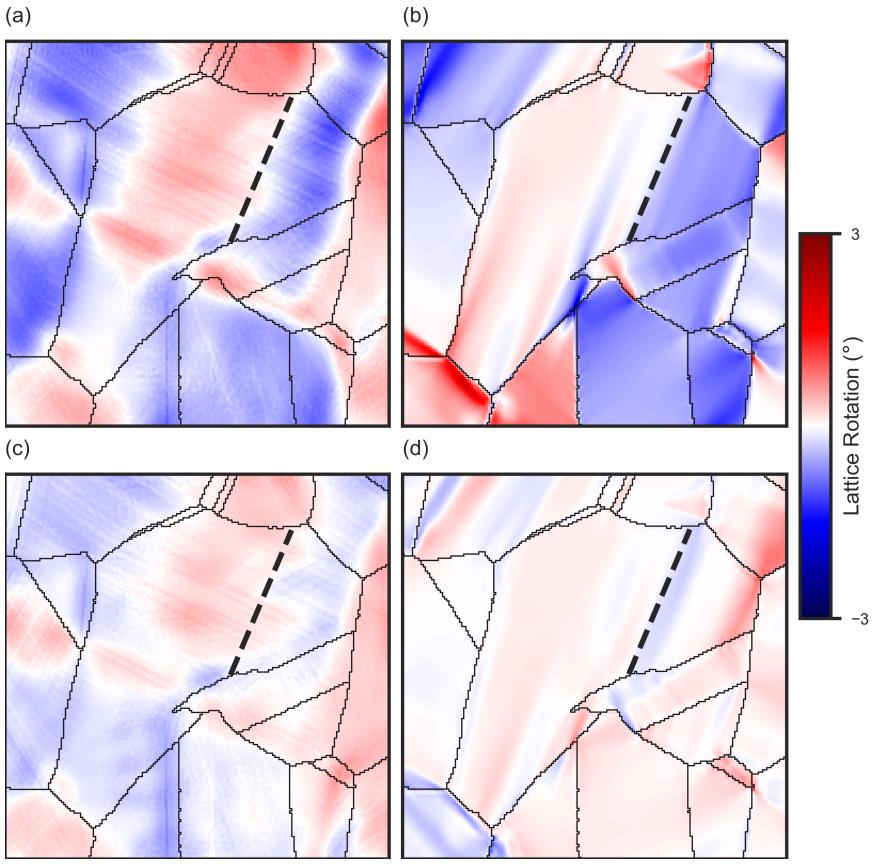

Figure 15: A second set of maps in the same microstructure of (a) experimental and (b) CPFE calculated lattice rotation after the first tension unload, and (c) experimental and (d) CPFE calculated lattice rotation maps after the first compression unload. The dashed line indicates the location of a polarized lattice rotation gradient.

3.5. Slip Localization

Slip bands producing high lattice rotation are of interest because they serve as precursors for crack initiation upon further cycling and they are commonly observed in IN718 and other Ni-based superalloys forming adjacent and parallel to, but not directly on, twin boundaries (TBs) [6]. We examine more closely the region of microstructure shown in Fig. 6 where this type of slip band is observed in experiment. To identify slip activity, slip localizations are measured using HR-DIC throughout this group of grains. Figure 18 shows the slip bands

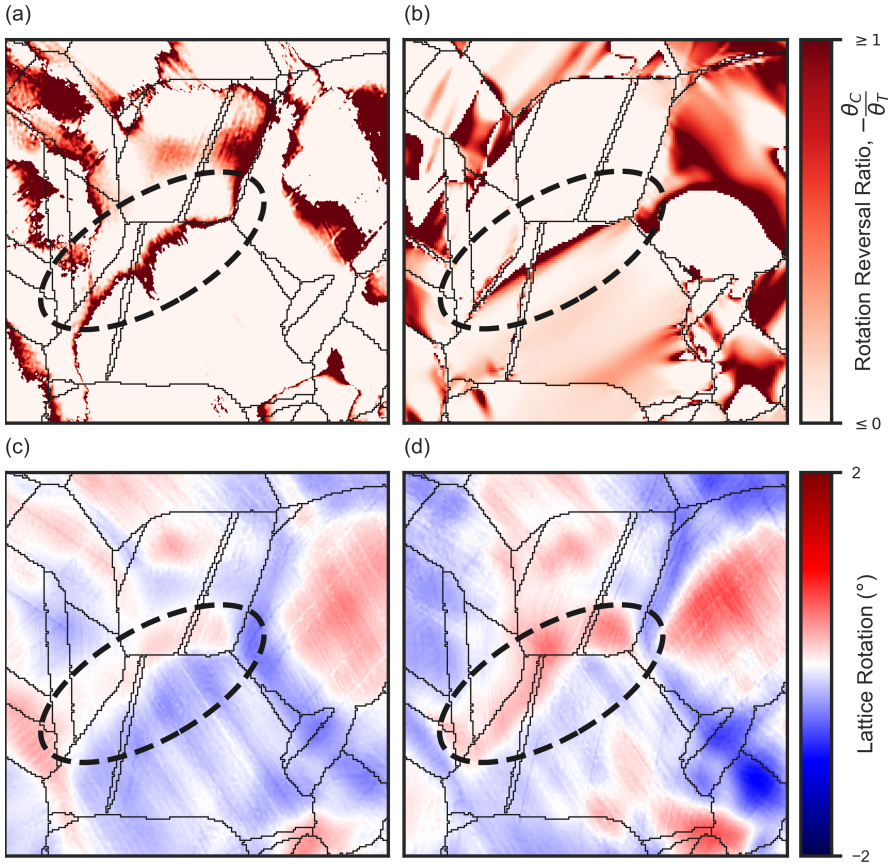

Figure 16: Maps of (a) experimental and (b) CPFE calculated lattice rotation reversal for the region of microstructure in Fig. 14 after the first compression unload. Experimental lattice rotation maps for the compression unload after (c) one and (d) 10 cycles. The dashed circle indicates the location of a polarized lattice rotation gradient that displays over-reversal and subsequent intensification with further cycling.

delineated by the HR-DIC analysis and a key indicating which slip planes they correspond to in this grain. Two separate regions of active dual slip are detected in experiment. One region extends over most of the grain interior, where many distinct slip bands in the form of $(\overline{1}11)$ slip traces are observed. Experimental analysis of their in-plane shearing angles (see ref. [14]) indicate they belong to systems C3:$(\overline{1}11)$ [101] and C5:$(\overline{1}11)$ [$\overline{1}$10]. The second smaller region spans the TB where the intense strain localization has developed. The band corresponds

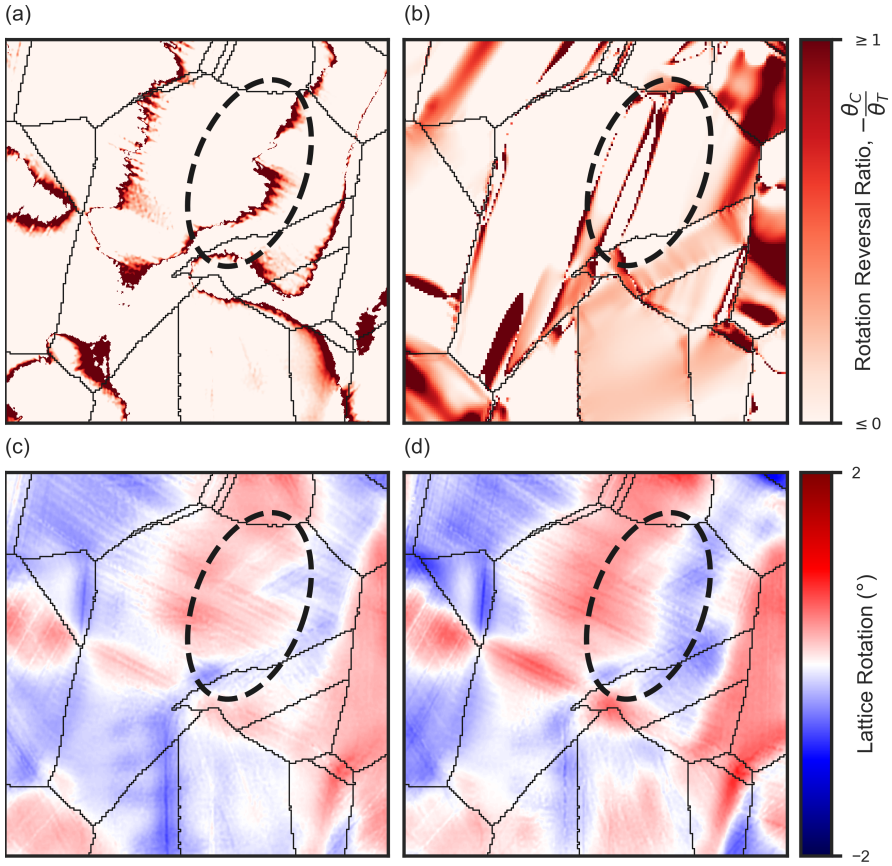

Figure 17: Maps of (a) experimental and (b) CPFE calculated lattice rotation reversal for the region of microstructure in Fig. 15 after the compression unload. Experimental lattice rotation maps for the compression unload after (c) one and (d) 10 cycles. The dashed circle indicates the location of a polarized lattice rotation gradient that displays over-reversal and subsequent intensification with further cycling.

to $(1\bar{1}1)$ slip traces and its shearing angles indicate mixed activity of systems D4:$(1\bar{1}1)\,[\bar{1}01]$ and D6:$(1\bar{1}1)\,[110]$. Like the entire microstructure, deformation of this grain is accomplished by activation of one or a pair of slip systems, in spatially distinct regions. Given that the orientation of this grain lies close to the $[011]-[\bar{1}11]$ boundary of the standard stereographic triangle, as can be seen in Fig. 1a, it would be expected that the coplanar slip systems C3 and C5 would be activated. However, the effect of the neighboring twin on activating locally

D4 and D6 is not taken into account and hence would not be anticipated.

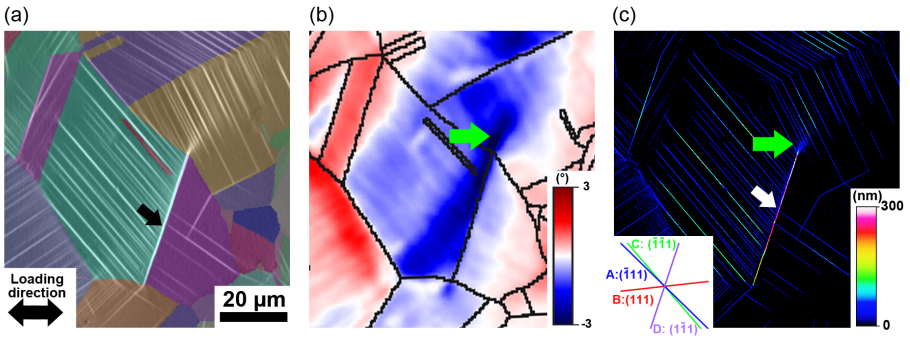

Figure 18: HR-DIC strain field overlaid on an EBSD map (a), experimental lattice rotation field (b), and in-plane slip displacement map (c) for a region of IN718 microstructure where intense slip localization (black and white arrows) and impingement (green arrow) is observed after uniaxial tension to 1.83% strain.

In Fig. 19, the slip activity calculated for this grain is indicated by the mean RSS value on each of the 12 systems, see Table 2 in Appendix for the designation of these slip systems. The negative sign of the RSS indicates that slip occurs in the opposing slip direction. In agreement, the model forecasts activity predominantly on systems C3:$(\bar{1}\bar{1}1)$ [101] and C5:$(\bar{1}\bar{1}1)$ [$\bar{1}$10]. It identifies the slip system D6:$(1\bar{1}\bar{1})$ [110] that created the strain localization as being active as well but secondary. Although the CPFE formulations in general are not capable of representing active slip spatially correlated in the form of an intense band, the CPFE model here does explain why the D6:$(1\bar{1}\bar{1})$ [110] slip system of the strain localization near the TB is not also prevalent over the entire grain.

Strain localizations near TBs, such as the one studied here, are found to not fully recover in cyclic loading, unlike the other slip bands in the same grain, far from the TB, which appear to recover [45]. The irreversibility of the localization is not yet fully understood. The mechanism could be driven by distinct changes in the slip redistribution that occur as the strain path changes from tension to compression. We carry out calculations in which the applied tensile deformation is followed by unloading and re-straining in reverse, refer to schematic in Fig. 9

with the five load steps. For this local region, we track the new slip activity by its RSS after the equivalent compression strain is reached (see 1-5C in Fig. 9).

By the end of compression, all systems experience some amount of reversal in RSS. To identify irreversible slip, the difference between RSS magnitudes at the end of compression reversal and the end of forward tension is evaluated for each slip system and shown in Fig. 19b. Positive differences in Fig. 19b indicate a full recovery of slip developed during the tensile load plus an additional increment of slip in the direction of compression i.e., increased slip activity in the compression strain path over that achieved during the tension strain path. Substantial amounts of additional slip increment during the compression strain path are found for systems D4:$(1\bar{1}1)\,[\bar{1}01]$ and D6:$(1\bar{1}1)\,[110]$ and less so on the primary active systems C3:$(\bar{1}11)\,[101]$ and C5:$(\bar{1}\bar{1}1)\,[\bar{1}10]$, as well as the other less active ones. The tendency to incur more slip on D6:$(1\bar{1}1)\,[110]$ than the other slip systems in the reload would suggest that the strain localization concentrated on this system would be irreversible during cyclic loading.

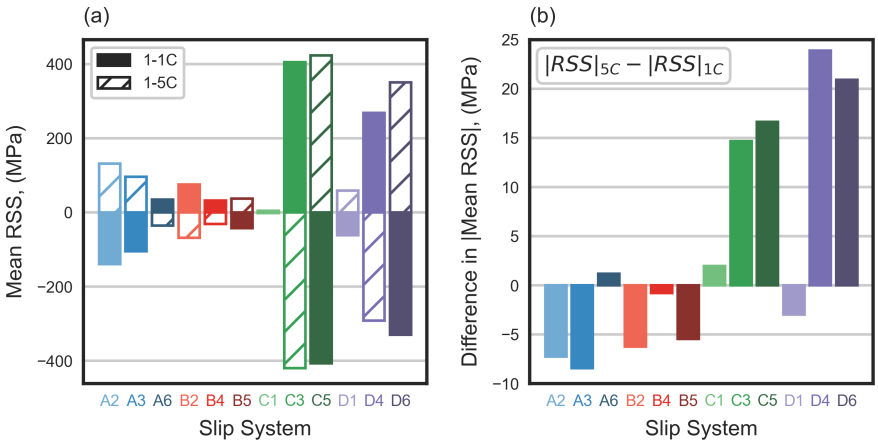

Figure 19: Mean RSS at states 1-1C and 1-5C (a), and difference in |mean RSS| between states (b) across individual slip systems for the grain of observed localization.

3.6. Sources of Discrepancies

In this work, measurements and calculations of inter- and intragranular lattice rotation for the same microstructure with the same high resolution were made, enabling point-to-point comparisons. Overall the model lattice distributions demonstrated good agreement, enabling us to carry out further analyses. However, qualitatively, we find that in a few portions of the microstructure, the lattice rotations were slightly larger and gradients sharper in the model than measurement.

These differences have been reported before in other studies comparing DIC and CPFE results [20, 22, 26, 46] and two reasons have been proposed, both of which apply to this study as well. First, we use a columnar microstructure, formed by extruding the experimental surface microstructure normal to the surface. In the absence of subsurface microstructure, some areas in the model could be less constrained than actuality, allowing easier development of lattice rotation. Grains are constrained to maintain compatibility with their neighboring grains. Unseen grains below the surface that are oriented to be either hard elastically or plastically or both will provide a greater constraint on the surface grains than those that are oriented to be softer. At present, the model assumes that the material below the surface grains has the same orientation. Because IN718 is elastically anisotropic, any difference in orientation between the subsurface grains and the studied surface grains can have an effect on the lattice rotations fields that develop. The second reason for the observed differences may be that the model's hardening law is too soft, not representing adequately the strain hardening that may develop in some regions of the material. For instance, GNDs could develop in response to gradients in lattice rotation and harden the material locally. Without additional GND hardening, this would likely result in larger rotations and sharper gradients than measured both after forward and reverse loading.

To quantify discrepancies here, the point-to-point differences in lattice rotation between the experiment and model maps for every element were calculated (see Fig. 21 in Appendix). This analysis indicates that as a fraction of all ele-

ments considered in the model, the discrepancies in lattice rotation are small. Also, larger differences in rotation occur more frequently at points closer to grain boundaries. The most frequently occurring difference is less than 0.5° and it occurs within 0.05 of the grain size from the grain boundary. Large differences near grain boundaries could be attributed to at least two factors. First, boundary-specific constitutive behavior is not included in the model, and second, brick elements, such as those used here, create "staircase-like" features at the grain boundaries producing minor artifacts in resolved fields, ultimately hindering analysis of elements with direct contact of these features. Choi et al. showed that staircase grain boundaries produce more extreme local plasticity as compared to smooth grain boundaries resulting in more extreme-value spots near the head and tail ends of distributions for quantities such as Mises stress, cumulative slip, and maximum slip [47].

While both the lack of subsurface microstructure and implementation of a simple hardening model likely contribute to the differences found between experiment and model lattice rotations, their relative contributions are not thought to be equal, with the former believed to play a dominating role. Work by Zhang et al. [46] studied the relative effects of subsurface microstructure, quasi-3d or realistic full-3D grain morphology, and choice of constitutive model parameters on resolved lattice orientation fields for polycrystalline Ti-5Al-2.5Sn. Two sets of constitutive model parameters were tested, with one set reversing the relative ease of prismatic and basal slip. It was found that grain morphology causes more substantial changes in the lattice reorientation than choice of constitutive parameters. The most convincing evidence presented here supporting subsurface microstructure as a dominant source of model discrepancy is the coexistence of mostly accurate regions with minimally inaccurate areas in lattice rotation. We speculate that regions showing good agreement coincide with subsurface microstructures that do not vary greatly with depth and/or have elastically compatible subsurface grain neighbors. The opposite may be true for regions which show strong disagreement with experiment. Further statistical analyses of subsurface microstructure and choice of hardening model are needed to guide

researchers towards developing more effective CPFE models.

4. Conclusions

In this work, we study the development of lattice rotations in a nickel-based superalloy microstructure under monotonic and cyclic loading using high-resolution digital image correlation (HR-DIC) and crystal plasticity finite element (CPFE). A generalized-plane stress CPFE model was created to simulate the traction-free surface conditions of the in-situ tension test sample. The resolutions of the measured and calculated data points are aligned and sufficiently high, permitting a full-field quantitative analysis of the inter- and intragranular in-plane lattice rotations. The calculations of grain-average response, local intragranular fields, gradients in rotation, and slip activity achieve reasonable agreement with experiment even at the subgrain scale. The main conclusions are as follows.

- The full range of intragranular lattice rotations in the sample develop primarily by activation of one to two active slip systems in each grain.
- Rare instances of highly multi-slip activity in the model ($>$ six active slip systems) are associated with noticeably low lattice rotation and high stress.
- The model points to the development of intragranular gradients in lattice rotation, not just exclusively at grain boundaries. Two types of gradients are observed, those with and without a sign change. Results of the model these gradient are associated with a change in the predominant slip system, involving coplanar and non-planar changes respectively.
- Grains preferentially accommodate deformation by activating a different set of slip systems in distinct parts of the grain rather than the same set of multiple slip systems uniformly throughout the grain. Comparisons of CPFE calculated and HR-DIC measured slip activity confirm the classical

model's ability to predict heterogeneously distributed slip activation and support the lattice rotation gradient analyses.

- Lattice rotation fields do not reverse perfectly between states of tension and compression even in the first load cycle, leading to irreversible changes in the grain-average rotation and grain-average misorientation distributions. Intragranular lattice rotation gradients marked by changes in sign increase in the reverse strain path and intensify with further cycling.

Acknowledgments

This work is funded by the U.S. Dept. of Energy, Office of Basic Energy Sciences Program DE-SC0018901.

References

[1] D. V. V. Satyanarayana, N. Eswara Prasad, Nickel-Based Superalloys, in: N. E. Prasad, R. J. H. Wanhill (Eds.), Aerospace Materials and Material Technologies : Volume 1: Aerospace Materials, Springer Singapore, Singapore, 2017, pp. 199–228. doi:10.1007/978-981-10-2134-3_9.
URL https://doi.org/10.1007/978-981-10-2134-3{_}9

[2] T. M. Pollock, S. Tin, Nickel-based superalloys for advanced turbine engines: chemistry, microstructure and properties, Journal of propulsion and power 22 (2) (2006) 361–374.

[3] J. C. Stinville, W. C. Lenthe, J. Miao, T. M. Pollock, A combined grain scale elastic-plastic criterion for identification of fatigue crack initiation sites in a twin containing polycrystalline nickel-base superalloy, Acta Materialia 103 (2016) 461–473. doi:10.1016/j.actamat.2015.09.050.
URL http://dx.doi.org/10.1016/j.actamat.2015.09.050

[4] D. Texier, J. Cormier, P. Villechaise, J.-C. Stinville, C. J. Torbet, S. Pierret, T. M. Pollock, Crack initiation sensitivity of wrought direct aged

alloy 718 in the very high cycle fatigue regime: the role of non-metallic inclusions, Materials Science and Engineering: A 678 (2016) 122–136. doi:https://doi.org/10.1016/j.msea.2016.09.098.
URL http://www.sciencedirect.com/science/article/pii/S0921509316311789

[5] M. A. Charpagne, J. C. Stinville, P. G. Callahan, D. Texier, Z. Chen, P. Villechaise, V. Valle, T. M. Pollock, Automated and quantitative analysis of plastic strain localization via multi-modal data recombination, Materials Characterization 163 (2020) 1–36. doi:10.1016/j.matchar.2020.110245.

[6] J. C. Stinville, W. C. Lenthe, M. P. Echlin, P. G. Callahan, D. Texier, T. M. Pollock, Microstructural statistics for fatigue crack initiation in polycrystalline nickel-base superalloys, International Journal of Fracture 208 (1-2) (2017) 221–240. doi:10.1007/s10704-017-0241-z.

[7] M. I. Latypov, J.-C. Stinville, J. R. Mayeur, J. M. Hestroffer, T. M. Pollock, I. J. Beyerlein, Insight into microstructure-sensitive elastic strain concentrations from integrated computational modeling and digital image correlation, Scripta Materialia 192 (2021) 78–82. doi:https://doi.org/10.1016/j.scriptamat.2020.10.001.
URL http://www.sciencedirect.com/science/article/pii/S1359646220306448

[8] J. Livingston, B. Chalmers, Multiple slip in bicrystal deformation, Acta Metallurgica 5 (6) (1957) 322 – 327. doi:https://doi.org/10.1016/0001-6160(57)90044-5.
URL http://www.sciencedirect.com/science/article/pii/0001616057900445

[9] B. Zhou, L. Wang, W. Liu, X. Zeng, Y. Li, Revealing the Subsurface Basal ⟨a⟩ Dislocation Activity in Magnesium Through Lattice Rotation Analysis, Metallurgical and Materials Transactions A: Physical Metallurgy and Materials Science 51 (9) (2020) 4414–4421. doi:10.1007/s11661-020-05907-w.

[10] M. Miller, C. Budrow, T. Long, M. Obstalecki, Understanding the evolving state of deforming polycrystals using synchrotron x-rays, IOP Conference Series: Materials Science and Engineering 580 (2019) 012009. doi:10.1088/1757-899x/580/1/012009.
URL https://doi.org/10.1088%2F1757-899x%2F580%2F1%2F012009

[11] F. Di Gioacchino, J. Quinta da Fonseca, An experimental study of the polycrystalline plasticity of austenitic stainless steel, International Journal of Plasticity 74 (2015) 92–109. doi:https://doi.org/10.1016/j.ijplas.2015.05.012.
URL https://www.sciencedirect.com/science/article/pii/S0749641915000820

[12] F. Roters, P. Eisenlohr, L. Hantcherli, D. Tjahjanto, T. Bieler, D. Raabe, Overview of constitutive laws, kinematics, homogenization and multiscale methods in crystal plasticity finite-element modeling: Theory, experiments, applications, Acta Materialia 58 (4) (2010) 1152 – 1211. doi:https://doi.org/10.1016/j.actamat.2009.10.058.
URL http://www.sciencedirect.com/science/article/pii/S1359645409007617

[13] A. Prakash, R. A. Lebensohn, Simulation of micromechanical behavior of polycrystals: finite elements versus fast fourier transforms, Modelling and Simulation in Materials Science and Engineering 17 (6) (2009) 064010. doi:10.1088/0965-0393/17/6/064010.
URL https://doi.org/10.1088%2F0965-0393%2F17%2F6%2F064010

[14] F. Bourdin, J. C. Stinville, M. P. Echlin, P. G. Callahan, W. C. Lenthe, C. J. Torbet, D. Texier, F. Bridier, J. Cormier, P. Villechaise, T. M. Pollock, V. Valle, Measurements of plastic localization by heaviside-digital image correlation, Acta Materialia 157 (2018) 307–325. doi:10.1016/j.actamat.2018.07.013.

[15] J. Stinville, M. Charpagne, F. Bourdin, P. Callahan, Z. Chen, M. Echlin,

D. Texier, J. Cormier, P. Villechaise, T. Pollock, V. Valle, Measurement of elastic and rotation fields during irreversible deformation using heaviside-digital image correlation, Materials Characterization (2020) 110600doi:https://doi.org/10.1016/j.matchar.2020.110600.
URL http://www.sciencedirect.com/science/article/pii/S1044580320320714

[16] M. Sachtleber, Z. Zhao, D. Raabe, Experimental investigation of plastic grain interaction, Materials Science and Engineering: A 336 (1-2) (2002) 81–87. doi:10.1016/S0921-5093(01)01974-8.
URL https://www.sciencedirect.com/science/article/pii/S0921509301019748

[17] T. Hoc, J. Crépin, L. Gélébart, A. Zaoui, A procedure for identifying the plastic behavior of single crystals from the local response of polycrystals, Acta Materialia 51 (18) (2003) 5477–5488. doi:10.1016/S1359-6454(03)00413-0.
URL https://www.sciencedirect.com/science/article/pii/S1359645403004130

[18] E. Héripré, M. Dexet, J. Crépin, L. Gélébart, A. Roos, M. Bornert, D. Caldemaison, Coupling between experimental measurements and polycrystal finite element calculations for micromechanical study of metallic materials, International Journal of Plasticity 23 (9) (2007) 1512–1539. doi:10.1016/J.IJPLAS.2007.01.009.
URL https://www.sciencedirect.com/science/article/pii/S074964190700006X

[19] Z. Zhao, M. Ramesh, D. Raabe, A. Cuitiño, R. Radovitzky, Investigation of three-dimensional aspects of grain-scale plastic surface deformation of an aluminum oligocrystal, International Journal of Plasticity 24 (12) (2008) 2278–2297. doi:10.1016/J.IJPLAS.2008.01.002.

URL https://www.sciencedirect.com/science/article/pii/S074964190800020X

[20] T. J. Turner, P. A. Shade, J. C. Schuren, M. A. Groeber, The influence of microstructure on surface strain distributions in a nickel micro-tension specimen, Modelling and Simulation in Materials Science and Engineering 21 (1). doi:10.1088/0965-0393/21/1/015002.

[21] H. Lim, J. D. Carroll, C. C. Battaile, T. E. Buchheit, B. L. Boyce, C. R. Weinberger, Grain-scale experimental validation of crystal plasticity finite element simulations of tantalum oligocrystals, International Journal of Plasticity 60 (2014) 1–18. doi:10.1016/j.ijplas.2014.05.004.
URL http://dx.doi.org/10.1016/j.ijplas.2014.05.004

[22] R. Pokharel, C. Hefferan, J. Lind, S. Lee, A. R. Ingraffea, A. D. Rollett, A. Cerrone, P. Kenesei, R. M. Suter, C. A. Stein, H. Tucker, T. Ozturk, Fatigue crack initiation, slip localization and twin boundaries in a nickel-based superalloy, Current Opinion in Solid State and Materials Sciencedoi:10.1016/j.cossms.2014.06.001.

[23] Z. Zhang, D. Lunt, H. Abdolvand, A. J. Wilkinson, M. Preuss, F. P. Dunne, Quantitative investigation of micro slip and localization in polycrystalline materials under uniaxial tension, International Journal of Plasticity 108 (April) (2018) 88–106. doi:10.1016/j.ijplas.2018.04.014.
URL https://doi.org/10.1016/j.ijplas.2018.04.014

[24] C. Tasan, J. Hoefnagels, M. Diehl, D. Yan, F. Roters, D. Raabe, Strain localization and damage in dual phase steels investigated by coupled in-situ deformation experiments and crystal plasticity simulations, International Journal of Plasticity 63 (2014) 198–210. doi:10.1016/J.IJPLAS.2014.06.004.
URL https://www.sciencedirect.com/science/article/pii/S0749641914001260

[25] K. Kapoor, Y. S. J. Yoo, T. A. Book, J. P. Kacher, M. D. Sangid, Incorporating grain-level residual stresses and validating a crystal plasticity model of a two-phase Ti-6Al-4-V alloy produced via additive manufacturing, Journal of the Mechanics and Physics of Solids 121 (2018) 447–462. doi:10.1016/J.JMPS.2018.07.025.
URL https://www.sciencedirect.com/science/article/pii/S0022509618300711

[26] A. Githens, S. Ganesan, Z. Chen, J. Allison, V. Sundararaghavan, S. Daly, Characterizing microscale deformation mechanisms and macroscopic tensile properties of a high strength magnesium rare-earth alloy: A combined experimental and crystal plasticity approach, Acta Materialia 186 (2020) 77 – 94. doi:https://doi.org/10.1016/j.actamat.2019.12.012.
URL http://www.sciencedirect.com/science/article/pii/S1359645419308419

[27] N. Zaafarani, D. Raabe, R. Singh, F. Roters, S. Zaefferer, Three-dimensional investigation of the texture and microstructure below a nanoindent in a cu single crystal using 3d ebsd and crystal plasticity finite element simulations, Acta Materialia 54 (7) (2006) 1863 – 1876. doi:https://doi.org/10.1016/j.actamat.2005.12.014.
URL http://www.sciencedirect.com/science/article/pii/S1359645406000292

[28] Y. Guan, B. Chen, J. Zou, T. B. Britton, J. Jiang, F. P. Dunne, Crystal plasticity modelling and HR-DIC measurement of slip activation and strain localization in single and oligo-crystal Ni alloys under fatigue, International Journal of Plasticity 88 (2017) 70–88. doi:10.1016/j.ijplas.2016.10.001.
URL http://dx.doi.org/10.1016/j.ijplas.2016.10.001

[29] A. D. Kammers, S. Daly, Self-assembled nanoparticle surface patterning

for improved digital image correlation in a scanning electron microscope, Experimental Mechanics 53 (2013) 1333–1341.

[30] J. Stinville, M. Echlin, D. Texier, F. Bridier, P. Bocher, T. Pollock, Sub-grain scale digital image correlation by electron microscopy for polycrystalline materials during elastic and plastic deformation, Experimental Mechanics (2015) 1–20doi:10.1007/s11340-015-0083-4.
URL http://dx.doi.org/10.1007/s11340-015-0083-4

[31] Z. Chen, W. Lenthe, J. Stinville, M. Echlin, T. Pollock, S. Daly, High-resolution deformation mapping across large fields of view using scanning electron microscopy and digital image correlation, Experimental Mechanics 58 (2018) 1407–1421. doi:Tttps://doi.org/10.1007/s11340-018-0419-y.

[32] S. Kalidindi, C. Bronkhorst, L. Anand, Crystallographic texture evolution in bulk deformation processing of FCC metals, Journal of the Mechanics and Physics of Solids 40 (3) (1992) 537–569. doi:10.1016/0022-5096(92)80003-9.
URL https://www.sciencedirect.com/science/article/pii/0022509692800039

[33] R. J. Asaro, Crystal Plasticity, Journal of Applied Mechanics 50 (4b) (1983) 921–934. arXiv:https://asmedigitalcollection.asme.org/appliedmechanics/article-pdf/50/4b/921/6362915/921_1.pdf, doi:10.1115/1.3167205.
URL https://doi.org/10.1115/1.3167205

[34] E. Marin, P. Dawson, On modelling the elasto-viscoplastic response of metals using polycrystal plasticity, Computer Methods in Applied Mechanics and Engineering 165 (1) (1998) 1–21. doi:https://doi.org/10.1016/S0045-7825(98)00034-6.
URL https://www.sciencedirect.com/science/article/pii/S0045782598000346

[35] L. Delannay, P. J. Jacques, S. R. Kalidindi, Finite element modeling of crystal plasticity with grains shaped as truncated octahedrons, International Journal of Plasticity 22 (10) (2006) 1879–1898. doi:https://doi.org/10.1016/j.ijplas.2006.01.008.
URL https://www.sciencedirect.com/science/article/pii/S0749641906000118

[36] S. L. Wong, M. Obstalecki, M. P. Miller, P. R. Dawson, Stress and deformation heterogeneity in individual grains within polycrystals subjected to fully reversed cyclic loading, Journal of the Mechanics and Physics of Solids 79 (2015) 157–185. doi:https://doi.org/10.1016/j.jmps.2015.03.010.
URL https://www.sciencedirect.com/science/article/pii/S0022509615000666

[37] D. Peirce, R. Asaro, A. Needleman, Material rate dependence and localized deformation in crystalline solids, Acta Metallurgica 31 (12) (1983) 1951 – 1976. doi:https://doi.org/10.1016/0001-6160(83)90014-7.
URL http://www.sciencedirect.com/science/article/pii/0001616083900147

[38] P. Franciosi, M. Berveiller, A. Zaoui, Latent hardening in copper and aluminium single crystals, Acta Metallurgica 28 (3) (1980) 273 – 283. doi:https://doi.org/10.1016/0001-6160(80)90162-5.
URL http://www.sciencedirect.com/science/article/pii/0001616080901625

[39] H. Mecking, U. Kocks, Kinetics of flow and strain-hardening, Acta Metallurgica 29 (11) (1981) 1865–1875. doi:https://doi.org/10.1016/0001-6160(81)90112-7.
URL http://www.sciencedirect.com/science/article/pii/0001616081901127

[40] G. Martin, N. Ochoa, K. Saï, E. Hervé-Luanco, G. Cailletaud, A multiscale model for the elastoviscoplastic behavior of Directionally

Solidified alloys: Application to FE structural computations, International Journal of Solids and Structures 51 (5) (2014) 1175–1187. doi:10.1016/J.IJSOLSTR.2013.12.013.
URL https://www.sciencedirect.com/science/article/pii/S0020768313004861

[41] M.-z. Wang, B.-x. Xu, Y. Gao, On the assumptions of the generalized plane stress problem and the filon average, Acta Mechanica 225 (4-5) (2014) 1419–1427, copyright - Springer-Verlag Wien 2014; Document feature - ; Last updated - 2020-12-03; CODEN - AMHCAP.
URL https://search.proquest.com/scholarly-journals/on-assumptions-generalized-plane-stress-problem/docview/1511169669/se-2?accountid=14522

[42] J. Nye, Some geometrical relations in dislocated crystals, Acta Metallurgica 1 (2) (1953) 153 – 162. doi:https://doi.org/10.1016/0001-6160(53)90054-6.
URL http://www.sciencedirect.com/science/article/pii/0001616053900546

[43] A. Arsenlis, D. Parks, Crystallographic aspects of geometrically-necessary and statistically-stored dislocation density, Acta Materialia 47 (5) (1999) 1597 – 1611. doi:https://doi.org/10.1016/S1359-6454(99)00020-8.
URL http://www.sciencedirect.com/science/article/pii/S1359645499000208

[44] S. Sun, B. L. Adams, W. E. King, Observations of lattice curvature near the interface of a deformed aluminium bicrystal, Philosophical Magazine A: Physics of Condensed Matter, Structure, Defects and Mechanical Properties 80 (1) (2000) 9–25. doi:10.1080/01418610008212038.

[45] J. C. Stinville, P. G. Callahan, M. A. Charpagne, M. P. Echlin, V. Valle, T. M. Pollock, Direct measurements of slip irreversibility in a nickel-based

superalloy using high resolution digital image correlation, Acta Materialia 186 (2020) 172–189. doi:10.1016/j.actamat.2019.12.009.

[46] C. Zhang, H. Li, P. Eisenlohr, W. Liu, C. Boehlert, M. Crimp, T. Bieler, Effect of realistic 3d microstructure in crystal plasticity finite element analysis of polycrystalline ti-5al-2.5sn, International Journal of Plasticity 69 (2015) 21–35. doi:https://doi.org/10.1016/j.ijplas.2015.01.003.
URL https://www.sciencedirect.com/science/article/pii/S074964191500011X

[47] Y. Choi, M. Groeber, T. Turner, D. Dimiduk, C. Woodward, M. Uchic, T. Parthasarathy, A crystal-plasticity fem study on effects of simplified grain representation and mesh types on mesoscopic plasticity heterogeneities, Materials Science and Engineering: A 553 (2012) 37–44. doi:https://doi.org/10.1016/j.msea.2012.05.089.
URL http://www.sciencedirect.com/science/article/pii/S0921509312007952

[48] E. Schmid, W. Boas, Kristallplastizität, 1st Edition, Springer-Verlag Berlin Heidelberg GmbH, Berlin, 1935.

Appendix

Table 2: {111}⟨110⟩ slip systems for FCC crystals with the notation of Schmid and Boas [48].

Slip System	Slip Plane Normal	Slip Direction
A2	$(\bar{1}11)$	$[0\bar{1}1]$
A3	$(\bar{1}11)$	$[101]$
A6	$(\bar{1}11)$	$[110]$
B2	(111)	$[0\bar{1}1]$
B4	(111)	$[\bar{1}01]$
B5	(111)	$[\bar{1}10]$
C1	$(\bar{1}\bar{1}1)$	$[011]$
C3	$(\bar{1}\bar{1}1)$	$[101]$
C5	$(\bar{1}\bar{1}1)$	$[\bar{1}10]$
D1	$(1\bar{1}1)$	$[011]$
D4	$(1\bar{1}1)$	$[\bar{1}01]$
D6	$(1\bar{1}1)$	$[110]$

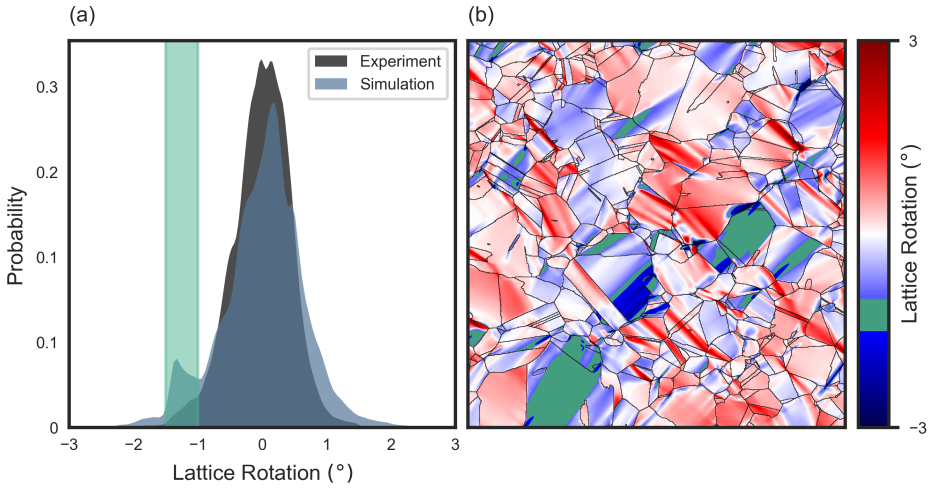

Figure 20: Probability density distributions of lattice rotation for experiment and simulation (a) with simulation sub-peak highlighted in green. CPFE calculated lattice rotation map (b), values inside sub-peak colored in green.

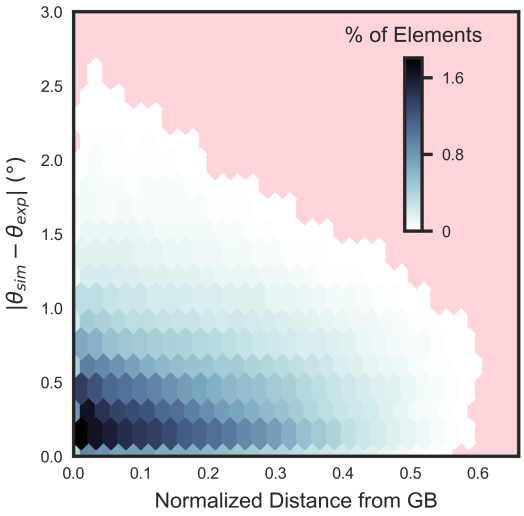

Figure 21: Bi-variate histogram of the absolute point-to-point difference in lattice rotation between simulation and experiment and the distance to the nearest grain boundary normalized by a material point's respective mean grain diameter.

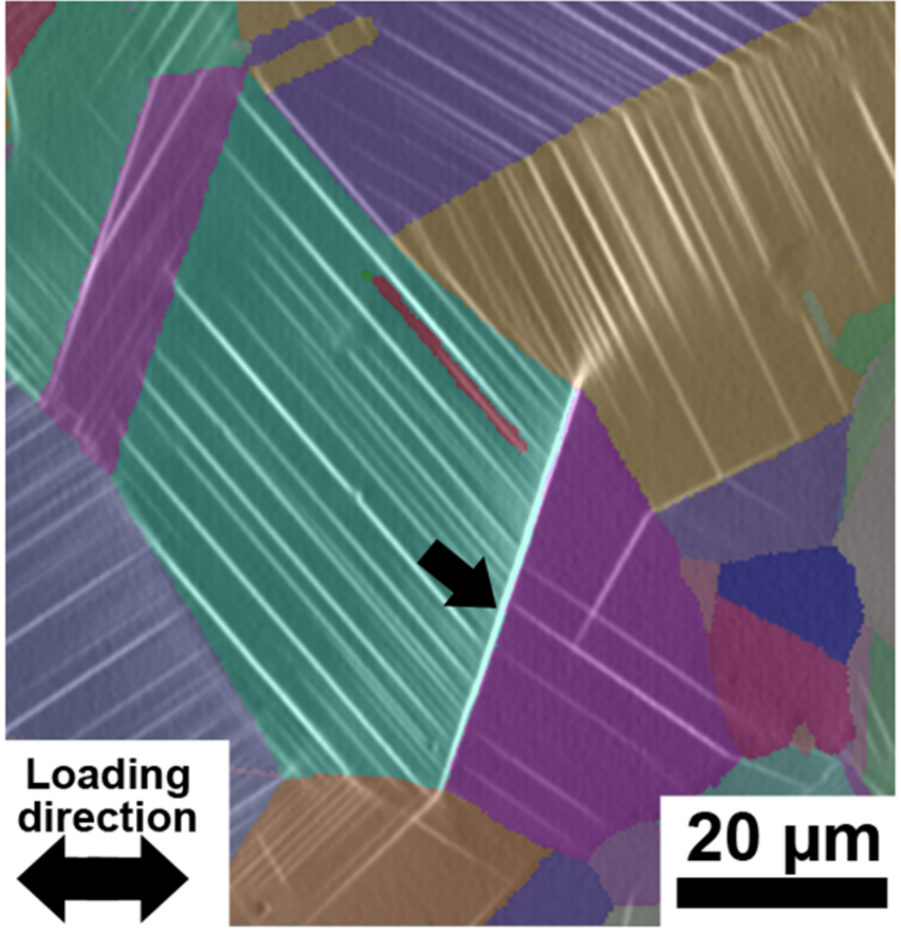
Loading
direction
20 µm

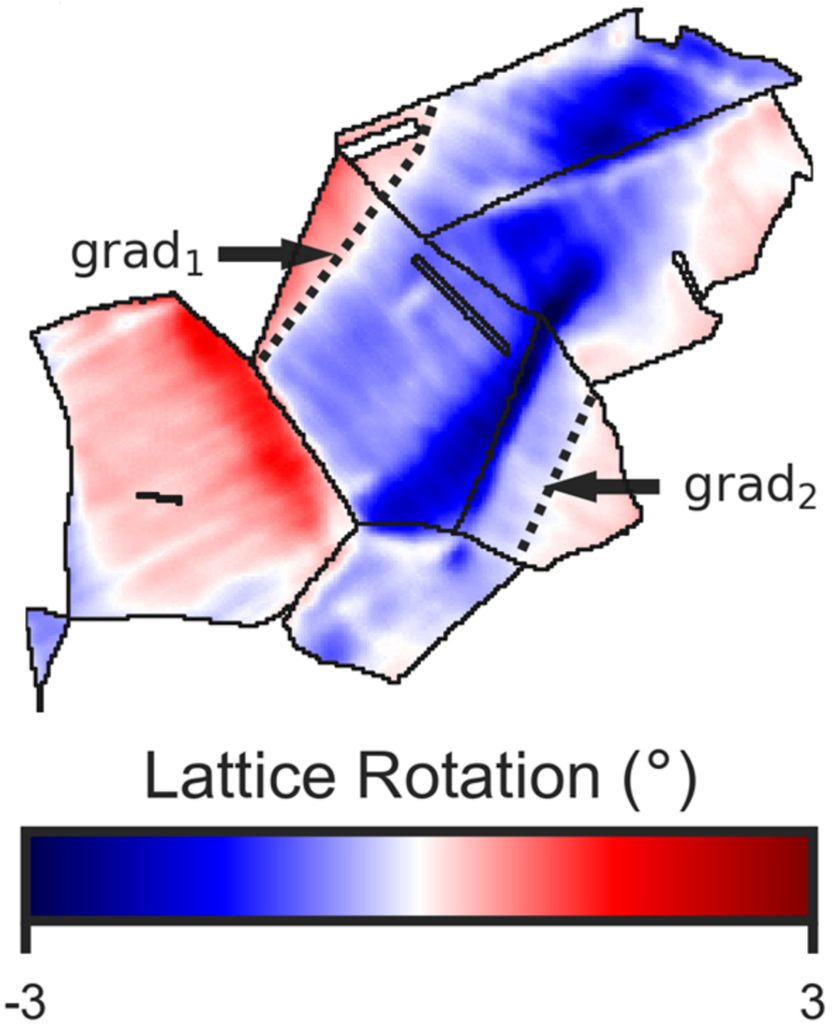
grad1
grad2
Lattice Rotation (°)
-3
3